The Astrophysical Journal Supplement Series, 247:27 (33pp), 2020 March https://doi.org/10.3847/1538-4365/ab6322

Swift Observations of Mrk 421 in Selected Epochs. III. Extreme X-Ray Timing/Spectral Properties and Multiwavelength Lognormality during 2015 December–2018 April

B. Kapanadze[1,2,3], A. Gurchumelia[2], D. Dorner[4], S. Vercellone[3], P. Romano[3], P. Hughes[5], M. Aller[5], H. Aller[5], and O. Kharshiladze[6]

[1] Ilia State University, Colokashvili Av. 3/5, Tbilisi, 0162, Georgia
[2] E. Kharadze National Astrophysical Observatory, Mt. Kanobili, Abastumani, 0803, Georgia
[3] INAF, Osservatorio Astronomico di Brera, Via E. Bianchi 46, I-23807 Merate, Italy
[4] Universität Würzburg, Institute for Theoretical Physics and Astrophysics, Emil-Fischer-Str. 31, D-97074 Würzburg, Germany
[5] Astronomy Department, University of Michigan, Ann Arbor, MI 48109-1107, USA
[6] I. Javakhishvili State University, Chavchavadze Av. 3, Tbilisi 0128, Republic of Georgia
Received 2019 September 5; revised 2019 November 25; accepted 2019 December 5; published 2020 March 5

Abstract

We present the results from the timing and spectral study of Mrk 421 based mainly on the *Swift* data in the X-ray energy range obtained during the time interval 2015 December–2018 April. The most extreme X-ray flaring activity on long-term, daily, and intraday timescales was observed during the 2 month period that started in 2017 December, when the 0.3–10 keV flux exceeded a level of 5×10^{-9} erg cm^{-2} s^{-1}, recorded only twice previously. While the TeV-band and X-ray variabilities were mostly correlated, the source often varied in a complex manner in the MeV–GeV and radio–UV energy ranges, indicating that the multifrequency emission of Mrk 421 could not always be generated in a single zone. The longer-term flares at X-rays and γ-rays showed a lognormal character, possibly indicating a variability imprint of the accretion disk onto the jet. A vast majority of the 0.3–10 keV spectra were consistent with the log-parabolic model, showing relatively low spectral curvature and correlations between the different spectral parameters, predicted in the case of the first- and second-order Fermi processes. The position of the synchrotron spectral energy distribution peak showed an extreme variability on diverse timescales between the energies $E_p < 0.1$ and >15 keV, with 15% of the spectra peaking at the hard X-ray, and was related to the peak height as $S^p \propto E_p^{\alpha}$ with $\alpha \sim 0.6$, which is expected for the transition from Kraichnan-type turbulence into the "hard sphere" one. The 0.3–300 GeV spectra showed features of the hadronic contribution, jet–star interaction, and upscatter in the Klein–Nishina regime in different time intervals.

Unified Astronomy Thesaurus concepts: Active galactic nuclei (16); X-ray active galactic nuclei (2035); Galaxy jets (601); Extragalactic astronomy (506)

Supporting material: figure set, machine-readable tables

1. Introduction

Blazars (BL Lacertae objects and flat-spectrum radio quasars) form the most violently variable class of active galactic nuclei, with timescales ranging from a few minutes (in the keV–TeV energy range) to several years (radio to optical frequencies). Moreover, BL Lacertae sources (BLLs) are characterized by featureless spectra, variable radio–optical polarization, compact radio structure, superluminal motion of some components, and a very broad continuum extending over the radio to the very high energy (VHE; $E > 100$ GeV) γ-ray energy ranges. The bolometric luminosity can occasionally reach a level of 10^{48} erg s^{-1}, particularly during the strong outbursts by the γ-ray emission (see Falomo et al. 2014). Consequently, BLLs are the most frequently detected class of extragalactic TeV sources (65 out of 82, with redshifts $z = 0.03$–0.61[7]) and form one of the most important constituents of the Large Area Telescope (LAT) 4 yr Point Source Catalog (3FGL; Acero et al. 2015). It is widely agreed that the extreme physical properties of BLLs are due to the beamed, nonthermal emission from a relativistic jet that is closely aligned with the observer's direction (estimated viewing angles $\theta < 10°$) and characterized by the bulk Lorentz factor $\Gamma \sim 10$, which occasionally attains values as high as $\Gamma \sim 50$ (Begelman et al. 2008).

In the $\log \nu$–$\log \nu F_\nu$ plane, BLLs generally demonstrate a double-humped, broadband spectral energy distribution (SED). There is a consensus that the lower-energy component (extended over radio to UV–X-ray frequencies) is produced by synchrotron emission of ultrarelativistic electrons (Celotti & Ghisellini 2008). A subclass of the high-energy-peaked BLLs (HBLs, peaking at UV–X-ray frequencies; Padovani & Giommi 1995 and references therein), are particularly important due to the disputed particle acceleration and cooling processes: their X-ray "budget" should be filled by synchrotron photons from the highest-energy leptons (electrons and, possibly, positrons), while the radiative lifetimes at these energies are very short (Massaro et al. 2004). Consequently, a detailed study of the timing and spectral behavior of these sources on diverse timescales reveals the most plausible acceleration mechanisms and allows us to draw conclusions about the physical properties of the jet emission region. Moreover, since the synchrotron and inverse Compton (IC) cooling are expected to be extremely important at these energies, the intense X-ray timing/spectral study of the nearby, bright HBLs may provide us with very important clues about the injection and radiative evolution of the freshly accelerated particles.

In this regard, the X-ray Telescope on board the *Neil Gehrels Swift Observatory* (*Swift*-XRT; Gehrels et al. 2004; Burrows et al. 2005) makes an outstanding contribution by performing

[7] http://tevcat.uchicago.edu/

regular monitoring of selected BLLs in their "visibility" periods, particularly during the densely sampled target-of-opportunity observations.[8] Owing to the excellent instrumental characteristics, good photon statistics, and low background counts of *Swift*-XRT, we are able to search for flux and spectral variability on diverse timescales (minutes to years), obtain high-quality spectra, and derive different spectral parameters for bright HBLs, even for exposures lasting a few hundred s.

The nearby ($z = 0.031$), TeV-detected HBL source Mrk 421 provides a unique X-ray space laboratory due to the following features (Balocovic et al. 2016; Kapanadze et al. 2016, 2018a, 2018b): (i) high brightness (with the *Swift*-XRT 0.3–10 keV count rates (CRs) >100 counts s^{-1}) during strong flares, corresponding to de-absorbed fluxes $F_{0.3-10\mathrm{keV}} \gtrsim 2.5 \times 10^{-9}$ erg cm^{-2} s^{-1}; (ii) exceptionally strong outbursts (e.g., in 2013 April; Pian et al. 2014; Kapanadze et al. 2016); (iii) very large and fast timing/spectral variability on timescales down to a few hundred s; and (iv) extremely hard spectra during strong flares with a photon index smaller than 1.6 and a synchrotron SED peak shifting beyond 10 keV, etc. Moreover, the source is also bright in other spectral ranges, making it a frequent target of densely sampled multiwavelength (MWL) campaigns (Macomb et al. 1995; Alecsic et al. 2012; Alecsic et al. 2015a, 2015b; Balocovic et al. 2016; etc.), which are crucial for checking the viability of models explaining the origin of the higher-energy SED component via the interband correlation study: (1) synchrotron self-Compton (SSC; scattering of synchrotron photons by their "parent" lepton population; Marscher & Gear 1985); (2) external Compton (EC), with the low-energy photons from the accretion disk (AD), dust torus, and narrow-/broad-line clouds upscattered by the jet ultra-relativistic particles (Dermer et al. 1992); and (3) hadronic models, which embody a generation of the keV–TeV emission by relativistic protons, either directly (synchrotron-proton scenario; Abdo et al. 2011) or indirectly (e.g., synchrotron radiation by the electron population, produced by a cascade induced by the interaction of high-energy protons with the ambient photons; Mannheim 1993). Despite the large number of publications related to the aforementioned observations, the details of the physical processes underlying the higher-energy SED component remain mainly unknown owing to (i) sparse MWL data during long periods, (ii) moderate or low sensitivity in the hard X-ray and γ-ray energy ranges in the past, and (iii) many previous MWL campaigns being triggered in the epochs of enhanced X-ray and γ-ray activity. Consequently, these studies are biased toward the high states of the source, while the distinct physical processes may play a dominant role during the moderate and lower brightness states.

For the aforementioned reasons, we performed a detailed study of X-ray spectral and flux variability in the MWL context, focused on the rich archival data obtained with XRT during 2005 March–2015 June (Kapanadze et al. 2016, 2017a, 2018a, 2018b). This campaign revealed extreme X-ray flares by a factor of 3–20 on timescales of a few days to weeks between the lowest historical state and that corresponding to a *Swift*-XRT rate higher than 200 counts s^{-1}. The source was characterized by extreme spectral and intraday flux variability, particularly during the strong flares. In the latter case, we were able to extract the 0.3–10 keV spectra for the time intervals of 50–100 s and explore the observational features predicted in the framework of the various particle acceleration and emission scenarios. The distribution of different spectral parameters and their cross-correlations hinted at the importance of the first- and second-order Fermi accelerations, changes in the turbulence type, possible hadronic contribution to the MeV–GeV emission, etc.

In this paper, we present the results of our detailed study of the timing/spectral behavior of Mrk 421 during the period 2015 December–2018 April, which was characterized by a very strong X-ray flare in the time interval 2017 December–2018 February and also showed intensive flaring activity in other parts of the presented period, revealed by the densely sampled *Swift*-XRT observations. Using XRT observations, we checked correlations between the 0.3 and 10 keV flux variability and those observed with different instruments: the Ultraviolet/Optical Telescope (UVOT; Roming et al. 2005) and the Burst Alert Telescope (BAT; Barthelmy et al. 2005) on board *Swift*, the LAT on board *Fermi* (Atwood et al. 2009), MAXI (Matsuoka et al. 2009), the First G-APD Cerenkov Telescope (FACT; Anderhub et al. 2013), the 40 m telescope of the Owens Valley Radio Observatory (OVRO; Richards et al. 2011), and the optical telescopes of Steward Observatory (Smith et al. 2009).

The paper is organized as follows. Section 2 encompasses the description of the data processing and analyzing procedures. The results of the X-ray and MWL timing study, as well as the X-ray spectral analysis, are presented in Section 3. We provide a discussion based on our results and the corresponding conclusions in Section 4. Finally, a summary of our study is given in Section 5.

2. Data Sets, Reduction, and Analysis

2.1. X-Ray Data

We retrieved the raw *Swift*-XRT data from NASA's Archive of Data on Energetic Phenomena[9] (HEASARC). The Level 1 event files were reduced, calibrated, and cleaned via the `XRTPIPELINE` script (included in the package `HEASOFT` v.6.26) by applying the standard filtering criteria and the latest calibration files of XRT CALDB v.20190412. The events with 0–2 grades are selected for those observations performed in the windowed-timing (WT) mode. The selection of the source and background extraction regions was performed with `XSELECT`, using the circular area with radii of 25–50 pixels depending on the source brightness and position in the XRT field of view (FOV), as well as on the exposure length. We produced a pileup correction for CR $\gtrsim 100$ counts s^{-1} by excluding the central area with radii of 1–3 pixels from the source extraction region, following the recipe provided by Romano et al. (2006). Afterward, the light curves were corrected using the task `XRTLCCORR` for the resultant loss of the effective area, bad/hot pixels, pileup, and vignetting. Moreover, the corrections on the point-spread function losses, different extraction regions, vignetting, and CCD defects were done by generating the ancillary response files (ARFs) using the `XRTMKARF` task.

Due to the high X-ray brightness of the source, it was generally not observed in the photon-counting regime. However, Mrk 421 was accidentally targeted in this regime three times in the presented period (ObsIDs 35014255,[10] 34228023, and 34228026). In those

[8] https://www.swift.psu.edu/toop/too.php

[9] https://heasarc.gsfc.nasa.gov/

[10] The three leading zeros of each ObsID are omitted throughout the paper.

cases, we used the events with 0–12 grades for our analysis. The pileup correction was done according to the prescription of Moretti et al. (2005). The radius, below which the model overproduced the data, was accepted as a region affected by pileup (11–15 pixels for the particular observation). The source events were extracted from an annular region with an inner radius encircling the pileup area and an outer radius of 50–60 pixels. The loss of counts caused by the inner hole in the source region, vignetting, and bad pixels was corrected by generating the corresponding ARF file. The background counts were extracted from a surrounding annulus with radii of 80 and 120 pixels.

From the publicly available, daily binned BAT[11] and MAXI[12] data, we used only those corresponding to the target's detection with a minimum significance of 5σ to study the variability of the 15–150 and 2–20 keV fluxes, respectively.

2.2. γ-Ray Observations

The reduction of the *Fermi*-LAT data was performed with `ScienceTools` (version v11r5p3), adopting the instrument response function `P8R3_SOURCE_V2` and the unbinned maximum-likelihood method `GTLIKE`. We selected the 0.3–300 GeV energy range for extraction of the photon flux and spectral information, since the effective area of the instrument is larger ($>0.5\,m^2$) and the angular resolution is relatively good (the 68% containment angle smaller than 2°) in that case (Atwood et al. 2009). Consequently, we obtain smaller systematic errors, and the spectral fit is less sensitive to possible contamination from unaccounted-for, transient neighboring sources (Abdo et al. 2011). The events of the diffuse class (`evclass` = 128, `evtype` = 3), i.e., those with the highest probability of being photons, from a region of interest (ROI) with the 10° radius centered at the location of Mrk 421 were included in our analysis. Moreover, we discarded the events at zenith angles >100° (to avoid contamination from the Earth-albedo photons generated by cosmic rays interacting with the upper atmosphere) and those recorded when the spacecraft rocking angle was larger than 52° (greatly reducing the contamination from Earth-limb photons).

The background model `gll_iem_v07.fits` was created to extract the γ-ray signal from (i) the Galactic diffuse emission component; (ii) an isotropic component, which is the sum of the extragalactic diffuse emission and the residual charged particle background (parameterized by the file `iso_P8R3_SOURCE_V2_v1.txt`); and (iii) all γ-ray sources from the *Fermi*-LAT 3FGL (Acero et al. 2015) within 20° of Mrk 421. For the spectral modeling of our target, we adopted a simple power law, similar to the 3FGL catalog. The spectral parameters of the sources within the ROI were left free during the minimization process, while those outside of this range were held fixed to the 3FGL catalog values. The normalizations of components (i) and (ii) in the background model were allowed to vary freely during the spectral fit. The photon flux and spectral parameters were estimated using the unbinned maximum-likelihood technique (Mattox et al. 1996).

When the target's detection significance is less than 5σ (i.e., the corresponding test statistics (TS) <25) and/or the number of model-predicted counts $N_{\rm pred} \lesssim 10$, such detections are not robust. For example, even a small change in the time bin width can result in significantly different values of the photon flux and spectral parameters. In such cases, we calculated the upper limit to the photon flux.[13]

We used the user-contributed tool `likeSED`[14] to construct the 300 MeV–300 GeV SED of Mrk 421. In that case, the photon indices of the sources were frozen to the best-fit values obtained from the full spectral analysis when performing unbinned likelihood fits in differential energy bins (following the recipe provided in Alecsic et al. 2015a).

The source was observed with FACT at VHEs during 363 nights for a total of 1408 hr in the period 2015 December 8–2018 April 8. For the timing study, we have used only the nightly binned TeV excess rates corresponding to detection significances higher than 3σ,[15] since more than 98% of these data are taken with a zenith distance small enough to not significantly influence the energy threshold of the analysis (see Dorner et al. 2015 for the data reduction and analysis details). More than 84% of the same data are taken under light conditions that do not increase the analysis threshold. This results in 190 nights for which the nightly observation time ranges from 0.66 to 7.32 hr. In the case of the 20 minute binned data, the source was detected 456 times in the presented period, and the corresponding rates were used in searching for the intraday brightness variability.

2.3. UV, Optical, and Radio Data

The source was targeted with *Swift*-UVOT in the ultraviolet bands *UVW1*, *UVM2*, and *UVW2* simultaneously with XRT. Generally, Mrk 421 was not observed with UVOT in the optical *V*–*U* bands due to the presence of very bright stars in the telescope's FOV. The absolute photometry for the sky-corrected images was performed by means of the `UVOTSOURCE` tool (distributed within `HEASOFT`) and the calibration files included in CALDB v.20170922. The measurements were done using a 20″ radius due to the target's high UV brightness. When the source was brighter than 12 mag, a pileup was estimated, and the corresponding correction was performed using the recipe provided in Page et al. (2013). According to the latter, a systematic uncertainty of ±0.1 mag should be added to the measurements. The magnitudes were then corrected for the Galactic absorption adopting $E(B-V) = 0.028$ mag (see Kapanadze et al. 2018a) and the $A_\lambda/E(B-V)$ values derived from the interstellar extinction curves (Fitzpartick & Messa 2007). For this purpose, we used the effective wavelength of each filter adopted from Poole et al. (2008). Finally, the magnitudes were converted into millijanskys by adopting the latest photometric zero-points for each band provided in Breeveld et al. (2011), and the host contribution was removed by subtracting the values of 0.09, 0.05, and 0.06 mJy for the *UVW1*, *UVM2*, and *UVW2* bands, respectively (Cesarini 2008).

The publicly available *V*- and *R*-band magnitudes, obtained with the 2.3 m Bock and 1.54 m Kuiper telescopes of Steward Observatory[16] (see Smith et al. 2009 for details), were dereddened and converted into millijanskys according to Bessel (1979). In both bands, the host contribution was subtracted following Fukugita et al. (1995) and Nilsson et al. (2007).

[11] http://swift.gsfc.nasa.gov/results/transients/weak/Mrk421/
[12] http://maxi.riken.jp/
[13] See fermi.gsfc.nasa.gov/ssc/data/analysis/scitools/upper_limits.html.
[14] https://fermi.gsfc.nasa.gov/ssc/data/analysis/user/
[15] See http://www.fact-project.org/monitoring/.
[16] See http://james.as.arizona.edu/~psmith/Fermi/.

The 15 GHz radio fluxes, obtained with the OVRO 40 m telescope, were retrieved from the corresponding website[17] (see Richards et al. 2011 for the data reduction and calibration steps). The sharp spikes or drops in the light curve, associated with less favorable observing conditions, were not included in our analysis.

2.4. Analysis Methods

The 0.3–10 keV spectra, extracted from the XRT observations and corrected for the different effects (see Section 2.1), were further reduced as follows. Using the GRPPHA task, we combined the instrumental channels to include at least 20 photons bin^{-1}, making a spectrum valid for the χ^2-statistics. The reduced spectra were fitted with three different models, generally adopted for the blazar X-ray spectra (by fixing the hydrogen column density to the Galactic value $N_H = 1.90 \times 10^{20}$ cm^{-2}, obtained within the Leiden/Argentine/Bonn survey; Kalberla et al. 2005): (1) the log-parabolic model (Massaro et al. 2004),

$$F(E) = K(E/E_1)^{-(a+b\log(E/E_1))}, \quad (1)$$

where E_1 is fixed to 1 keV, a is the photon index at the energy E_1, b is the curvature parameter, K is the normalization factor, and the position of the synchrotron SED peak was calculated as $E_p = 10^{(2-a)/2b}$ keV; (2) a simple power law $F(E) = KE^{-\Gamma}$, where Γ is the photon index throughout the entire 0.3–10 keV energy range; and (3) a broken power law,

$$F(E) = KE^{-\Gamma_1}, \ E \leqslant E_{br}$$
$$F(E) = KE_{br}^{\Gamma_2-\Gamma_1}(E/1keV)^{-\Gamma_2}, \ E > E_{br}, \quad (2)$$

where E_{br} is the break point for the energy in keV, Γ_1 is the photon index for $E \leqslant E_{br}$, and Γ_2 is the photon index for $E \leqslant E_{br}$. The model validity was determined using the reduced χ^2 (χ^2_r), distribution of the residuals, and F-test. The high X-ray brightness of Mrk 421 allowed us to extract the spectra from separate orbits of the particular ObsID (especially important when it is impossible to use the same source and/or background extraction regions for all orbits or the source is variable), or even from the separated segments of a single orbit in the medium and higher brightness states. The unabsorbed 0.3–2, 2–10, and 0.3–10 keV fluxes and their errors (in logarithmic units) were derived using the task EDITMOD.

The hardness ratio (HR) was determined as $HR = F_{2-10\,keV}/F_{0.3-2\,keV}$, where $F_{2-10\,keV}$ and $F_{0.3-2\,keV}$ stand for the de-absorbed 2–10 and 0.3–2 keV fluxes, respectively.

In order to study the statistical properties of different spectral parameters, we constructed a histogram and normalized cumulative distribution for the values of each parameter. A Kolmogorov–Smirnov (K-S) test was adopted to compare the distributions of the particular parameter in different time intervals, defined in Table 1, and measure the distance $D_{K\text{-}S}$ between the normalized cumulative distributions of parameters corresponding to the two different periods, following the recipe provided by Massaro et al. (2011a). Since our samples are not statistically complete, a comparison of the corresponding distributions can be affected by biases, and there is a risk of obtaining a large $D_{K\text{-}S}$ value between the selected cumulative distributions indicating that they are different, simply due to the lack/absence of data in some particular bins of each histogram. To check the significance of the results provided by the K-S test, we adopted a method based on the Monte Carlo simulations (developed by Massaro et al. 2011a) to account for this effect and estimate its relevance. First, we performed the K-S test and derived the $D_{K\text{-}S}$ quantity for two normalized cumulative distributions. Afterward, we randomly simulated two distributions for both data sets with the same number of components, adopting two different shapes for the simulated distributions, log-uniform and lognormal, the former simply having the same maximum and minimum values of the observed distribution and the latter having the same variance and median of the observed distribution and spanning the same range of values. We measured the $D_{K\text{-}S,simul}$ distance between the simulated distributions, repeated the simulations at least 30,000 times, and built a distribution of the obtained $D_{K\text{-}S,simul}$. Finally, we estimated the probability of obtaining the observed $D_{K\text{-}S}$ randomly, which provides the confidence level of our K-S test.

Table 1
The Intervals and Subintervals Referred to Throughout the Paper

Period	Dates	MJD
1	2015 Dec 8 to 2016 Jun 16	57,364–57,555
1a	2015 Dec 8 to 2016 Feb 4	57,364–57,422
1b	2016 Feb 6 to 2016 Jun 16	57,424–57,555
2	2016 Nov 25 to 2017 Jun 27	57,717–57,931
2a	2016 Nov 25 to 2017 Jan 29	57,717–57,782
2b	2017 Jan 31 to 2017 Jun 27	57,784–57,931
3	2017 Dec 3 to 2018 Apr 8	58,090–58,216
3a	2017 Dec 16 to 2018 Feb 19	58,103–58,168
3b	2018 Feb 21 to 2018 Apr 8	58,170–58,216

For each variability instance, we calculated the fractional variability amplitude and its error according to Vaughan et al. (2003),

$$F_{var} = (S^2 - \overline{\sigma^2_{err}})^{1/2}/\overline{F}$$
$$\mathrm{err}(F_{var}) = \left\{\left(\sqrt{\frac{1}{2N}}\frac{\overline{\sigma^2_{err}}}{\overline{x}^2 F_{var}}\right)^2 + \left(\sqrt{\frac{\overline{\sigma^2_{err}}}{N}}\frac{1}{\overline{x}}\right)^2\right\}^{1/2}, \quad (3)$$

where S^2 is the sample variance, $\overline{\sigma^2_{err}}$ is the mean square error, and $\overline{F}$ is the mean flux.

In order to investigate the possible quasi-periodical behavior of the flux variations, we first constructed the Lomb–Scargle (LSP) periodogram (Lomb 1976; Scargle 1982), which is an improved Fourier-based technique suitable for unevenly sampled time series g_n without interpolation for the data gaps (VanderPlas 2018),

$$P(f) = \frac{A^2}{2}\left(\sum_n g_n \cos(2\pi f[t_n - \tau]\right)^2 + \frac{A^2}{2}\left(\sum_n g_n \sin(2\pi f[t_n - \tau]\right)^2, \quad (4)$$

where A, B, and τ are arbitrary functions of the frequency f and observing times $\{t_i\}$. The LSP yields the most significant spectral power peak and estimates its significance level by testing the false-alarm probability of the null hypothesis.

[17] See http://www.astro.caltech.edu/ovroblazars/.

Table 2
Summary of the XRT and UVOT Observations in the Time Interval 2015 December–2018 April

ObsID	Obs. Start–End (UTC)	MJD	Exp. (s)	CR (counts s^{-1})	*UVW1* (mag)	*UVW1* (mJy)	*UVM2* (mag)	*UVM2* (mJy)	*UVW2* (mag)	*UVW2* (mJy)
(1)	(2)	(3)	(4)	(5)	(6)	(7)	(8)	(9)	(10)	(11)
35014240	2015 Dec 8 10:15:58–11:22:39	57,364.431	1015	7.11(0.09)	11.53(0.11)	21.79(0.79)	11.72(0.04)	15.65(0.28)	11.51(0.10)	18.31(0.46)
35014241	2015 Dec 11 11:38:58–12:43:43	57,367.487	959	21.14(0.15)	11.78(0.10)	17.29(0.63)	11.90(0.04)	13.25(0.28)	11.80(0.03)	14.00(0.28)
35014242	2015 Dec 14 09:56:58–11:02:04	57,370.416	1069	49.04(0.22)	11.47(0.11)	23.03(0.79)	11.67(0.04)	16.39(0.28)	11.47(0.10)	18.99(0.46)
35014243	2015 Dec 17 11:20:58–12:26:26	57,373.475	1015	43.58(0.21)	11.54(0.11)	21.59(0.79)	11.76(0.04)	15.09(0.28)	11.49(0.10)	18.65(0.46)
35014245	2015 Dec 18 04:50:58–23:29:49	57,374.204	5892	29.34(0.14)	11.49(0.10)	22.61(0.74)	11.66(0.10)	16.55(0.38)	11.50(0.10)	18.48(0.41)

Note. See the corresponding machine-readable table for the entire table. The columns are as follows: (1) observation ID; (2) observation start–end; (3) Modified Julian Date corresponding to the observation start; (4) exposure (in seconds); (5) observation-binned 0.3–10 keV CR and associated uncertainty shown in parentheses; (6)–(11) dereddened UVOT magnitudes and corresponding fluxes (in mJy).

(This table is available in its entirety in machine-readable form.)

Table 3
Summary of the XRT and UVOT Observations in Different Intervals

XRT												
	0.3–10 keV				0.3–2 keV				2–10 keV			
Per. (1)	CR_{max} (2)	$\Re$ (3)	Mean (4)	$100 \times F_{var}$ (5)	F^{max} (6)	$\Re$ (7)	Mean (8)	$100 \times F_{var}$ (9)	F_{max} (10)	$\Re$ (11)	Mean (12)	$100 \times F_{var}$ (13)
1	95.72(0.32)	13.5	31.53(0.02)	50.5(0.1)	15.85(0.18)	12.3	7.19(0.01)	41.6(0.1)	13.93(0.38)	59.5	3.55(0.01)	75.0(0.2)
1a	67.83(0.28)	9.5	37.98(0.03)	35.4(0.1)	12.76(0.26)	9.9	7.60(0.01)	30.3(0.1)	7.96(0.24)	34.0	3.31(0.01)	44.5(0.3)
1b	95.72(0.32)	11.4	26.56(0.03)	60.3(0.1)	15.85(0.18)	8.3	6.62(0.01)	55.9(0.1)	13.93(0.38)	46.3	38.90(0.01)	95.9(0.4)
2	63.75(0.30)	9.0	25.81(0.02)	44.5(0.1)	12.02(0.14)	7.9	5.54(0.01)	34.2(0.1)	12.25(0.33)	47.5	38.24(0.01)	58.8(0.2)
2a	55.70(0.18)	7.9	21.40(0.03)	62.4(0.1)	9.66(0.15)	6.4	5.45(0.01)	39.7(0.1)	9.33(0.25)	36.2	37.70(0.01)	65.8(0.4)
2b	63.75(0.30)	4.2	28.43(0.03)	33.5(0.1)	12.02(0.14)	4.2	5.61(0.01)	30.1(0.1)	12.25(0.33))	12.7	38.62(0.01)	53.9(0.3))
3	162.88(0.70)	8.5	60.89(0.03)	51.0(0.1)	26.85(0.30)	13.2	14.29(0.01)	38.8(0.01)	29.04(0.79)	31.2	11.80(0.02)	63.4(0.2)
3a	162.88(0.70)	7.1	71.26(0.04)	45.9(0.1)	26.85(0.30)	6.1	15.60(0.01)	33.5(0.01)	29.04(0.79)	22.1	13.30(0.02)	55.6(0.2)
3b	61.10(0.26)	3.2	43.33(0.05)	27.2(0.1)	19.45(0.27)	9.6	8.52(0.01)	38.5(0.02)	10.38(0.32)	11.1	5.15(0.02)	40.4(0.4)

UVOT												
	UVW1				*UVM2*				*UVW2*			
Per. (14)	F_{max} (15)	$\Re$ (16)	Mean (17)	$100 \times F_{var}$ (18)	F_{max} (19)	$\Re$ (20)	Mean (21)	$100 \times F_{var}$ (22)	F_{max} (23)	$\Re$ (24)	Mean (25)	$100 \times F_{var}$ (26)
1	29.83(1.05)	2.4	22.8(0.4)	20.36(0.07)	21.22(0.41)	2.1	15.19(0.03)	21.3(0.2)	26.24(0.74)	2.4	18.10(0.05)	23.0(0.3)
1a	28.75(0.97)	1.7	22.86(0.13)	12.5(0.6)	20.64(0.28)	1.7	15.88(0.04)	16.5(0.3)	26.24(0.74)	1.9	20.09(0.07)	15.1(0.4)
1b	29.83(1.05)	2.4	18.15(0.09)	26.5(0.5)	21.22(0.41)	2.1	14.55(0.03)	25.0(0.3)	25.06(0.64)	2.3	16.16(0.06)	26.1(0.4)
2	18.11(0.63)	2.1	11.33(0.04)	18.4(0.3)	11.11(0.19)	2.7	7.73(0.02)	20.0(0.2)	14.13(0.28)	1.9	9.90(0.02)	14.9(0.2)
2a	18.11(0.63)	2.1	12.8(0.07)	19.9(0.6)	11.11(0.19)	2.7	7.56(0.03)	28.2(0.4)	14.13(0.28)	1.9	10.65(0.04)	17.1(0.4)
2b	13.71(0.50)	1.5	10.38(0.04)	7.9(0.04)	10.51(0.19)	1.9	7.84(0.02)	13.1(0.3)	13.00(0.28)	1.7	9.42(0.03)	10.1(0.3)
3	25.50(0.64)	2.1	19.40(0.07)	20.1(0.4)	18.82(0.28)	2.0	13.6(0.03)	17.2(0.2)	22.43(0.56)	2.0	17.16(0.04)	19.0(0.3)
3a	25.50(0.64)	1.4	21.82(0.10)	7.2(0.5)	18.82(0.28)	1.6	14.92(0.04)	10.8(0.3)	22.43(0.56)	1.4	19.29(0.06)	7.1(0.3)
3b	19.14(0.63)	1.6	14.10(0.10)	14.8(0.7)	15.08(0.28)	1.6	11.17(0.04)	12.1(0.4)	17.64(0.41)	1.6	12.99(0.06)	13.1(0.5)

Note. Cols(2)–(5): maximum 0.3–10 keV flux (in counts s^{-1}), maximum-to-minimum flux ratio, mean flux (in counts s^{-1}) and fractional amplitude, respectively; maximum de-absorbed flux (in 10^{-10} erg cm^{-2} s^{-1}), maximum-to-minimum flux ratio, mean flux (in 10^{-10} erg cm^{-2} s^{-1}) and fractional amplitude in the 0.3–2 keV (Cols((6)–(9)) and 2–10 keV (Cols(10)–(13)) bands; maximum unabsorbed flux (in mJy), maximum-to-minimum flux ratio, mean flux (in mJy), and fractional amplitude in the bands *UVW1* (Cols(15)–(18)), *UVM2* (Cols(19)–(22)) and *UVW2* (Cols(23)–(26)).

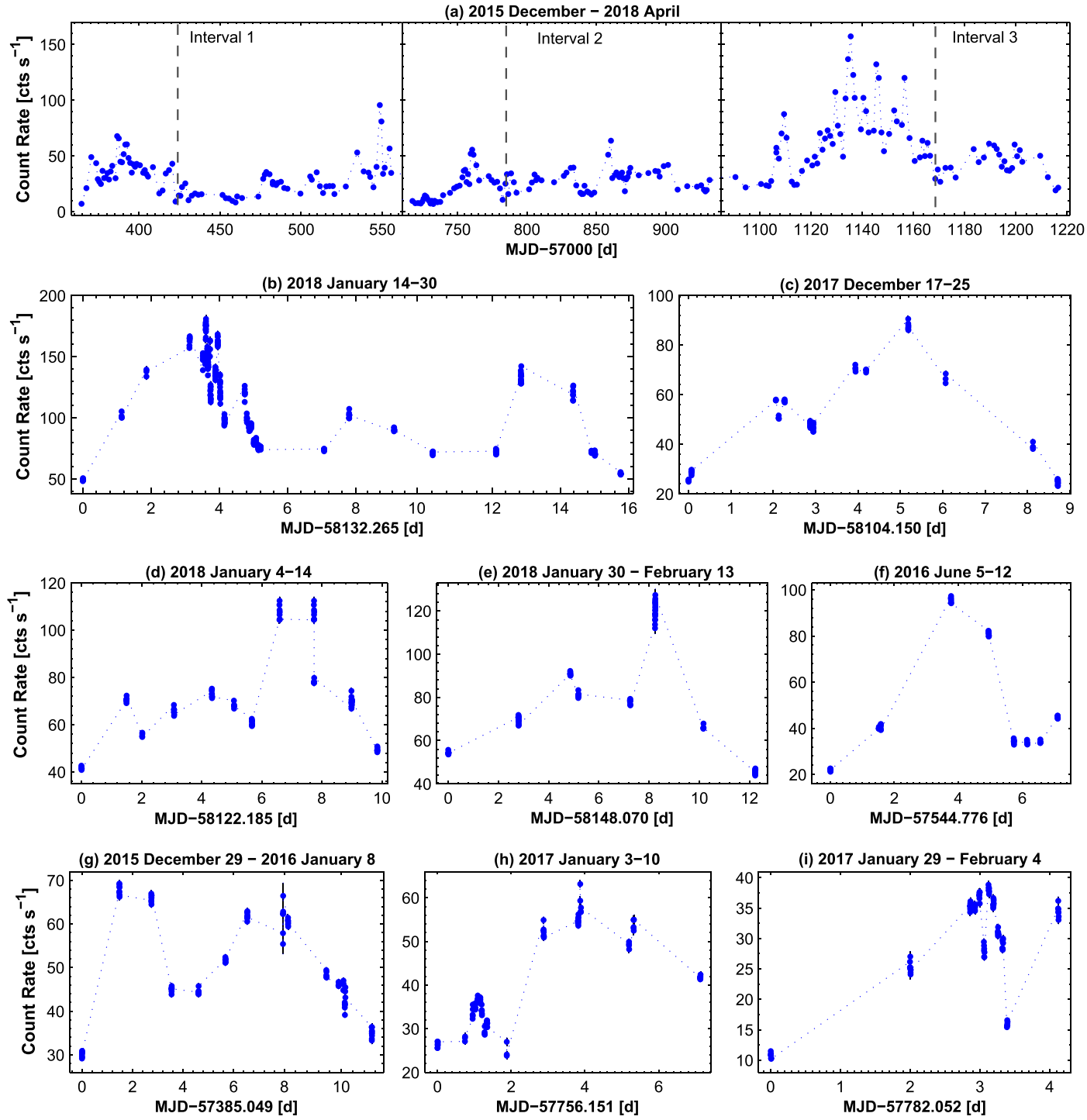

Figure 1. Panel (a): X-ray flaring activity of Mrk 421 in the 0.3–10 keV energy range during different periods. In each plot, the vertical dashed line denotes a boundary between the different subintervals. Panels (b)–(i): the strongest X-ray flares during intervals 1–3.

Foster (1996) introduced the weighted wavelet Z-transform (WWZ) method, which is a periodicity analysis technique in both the time and frequency domains. Note that WWZ is suited for discovering variability timescales and robust against missing data. It is defined as

$$\mathrm{WWZ} = \frac{(N_{\mathrm{eff}} - 3)V_{\mathrm{y}}}{2(V_{\mathrm{x}} - V_{\mathrm{y}})}, \tag{5}$$

where N_{eff} is the so-called effective number of data points, and V_{x} and V_{y} are the weighted variation of the data $x(t)$ and model function $y(t)$, respectively. The WWZ is based on the Morlet wavelet (Grossmann & Morlet 1984) $f(z) = e^{-cz^2}(e^{iz} - e^{-1/4c})$, where the constant $e^{-1/4c}$ is inserted so that the wavelet's mean value is zero.

Throughout the paper, the errors are quoted at the 90% confidence level for the one parameter of interest, unless otherwise stated.

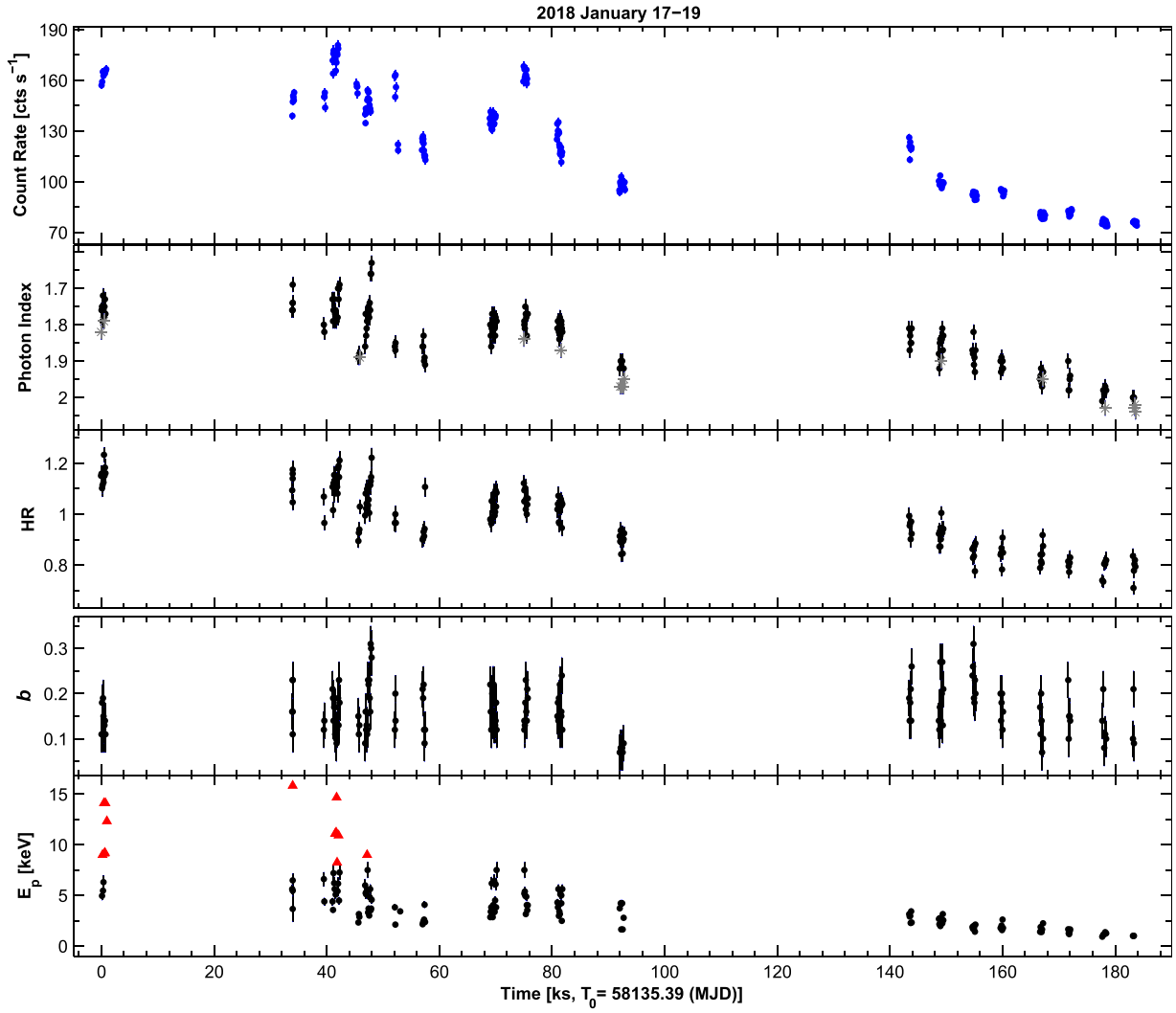

Figure 2. Top panel: intraday 0.3–10 keV variability during the strongest X-ray flaring activity in 2018 January 17–19. The subsequent panels show the timing behavior of different spectral parameters. In the second panel, the black points and gray asterisks stand for the photon indices a and Γ, respectively. Red triangles in the bottom panel stand for the lower limits to the intrinsic position of the synchrotron SED peak.

Table 4
The 0.3–10 keV IDVs during 2015 December–2018 April

ObsID (1)	MJD/ΔT (hr) (2)	χ^2_r/dof/bin (3)	100 × F_{var} (4)	a or Γ (5)	b (6)	E_p (keV) (7)	HR (8)	Remark (9)
35014242	57,370.416/0.30	3.41/ 8/120 s	2.1(0.5)	2.20(0.02) −2.24(0.02)	0.38(0.04) −0.44(0.04)	0.50(0.06) −0.58(0.07)	0.41(0.01) −0.44(0.02)	1
34014243− 31202245 Or1	57,373.475/17.98	2925/1/Or	26.3(0.3)	2.17(0.02) −2.31(0.02)	0.20(0.05) −0.27(0.05)	0.21(0.04) −0.48(0.06)	0.38(0.01) −0.51(0.02)	1, 3
35014245	57,374.204/18.66	28.63/5/Or	3.4(0.3)	2.28(0.02)−2.36 (0.02)LP 2.31(0.02)PL	0.13(0.04) −0.23(0.04)	0.05(0.02) −0.24(0.05)	0.38(0.01) −0.45(0.02)	1, 2, 4, 5
35014245 Or1	57,374.204/0.48	2.82/ 18/90 s	2.7(0.5)	2.31(0.02) −2.36(0.02)	0.14(0.04) −0.23(0.04)	0.05(0.02) −0.21(0.04)	0.38(0.01) −0.42(0.02)	1, 2, 4

Note. See the corresponding machine-readable table for the full version. Col. (1): ObsIDs of the *Swift*-XRT pointings to the source during which the given event was recorded. Col. (2): MJD of the observation start and total length of the particular observation (including the intervals between the separate orbits). Col. (3): reduced χ^2 and corresponding degrees of freedom for the given observations, along with the time bin used for the variability search. Col. (4): fractional variability amplitude and associated error in parentheses. Cols. (5)–(8): ranges of different spectral parameters, obtained via the log-parabolic (LP) or power-law (PL) fits with the spectra extracted from the separate orbits (or segments) of the corresponding XRT observation. Col. (9): remark related to the variable spectral parameter making the basic contribution in the observed IDV: 1—photon index; 2—curvature; 3—E_p; 4—S_p; 5—change in the particles' energy distribution from the log-parabolic functional shape into the power-law one or vice versa.

(This table is available in its entirety in machine-readable form.)

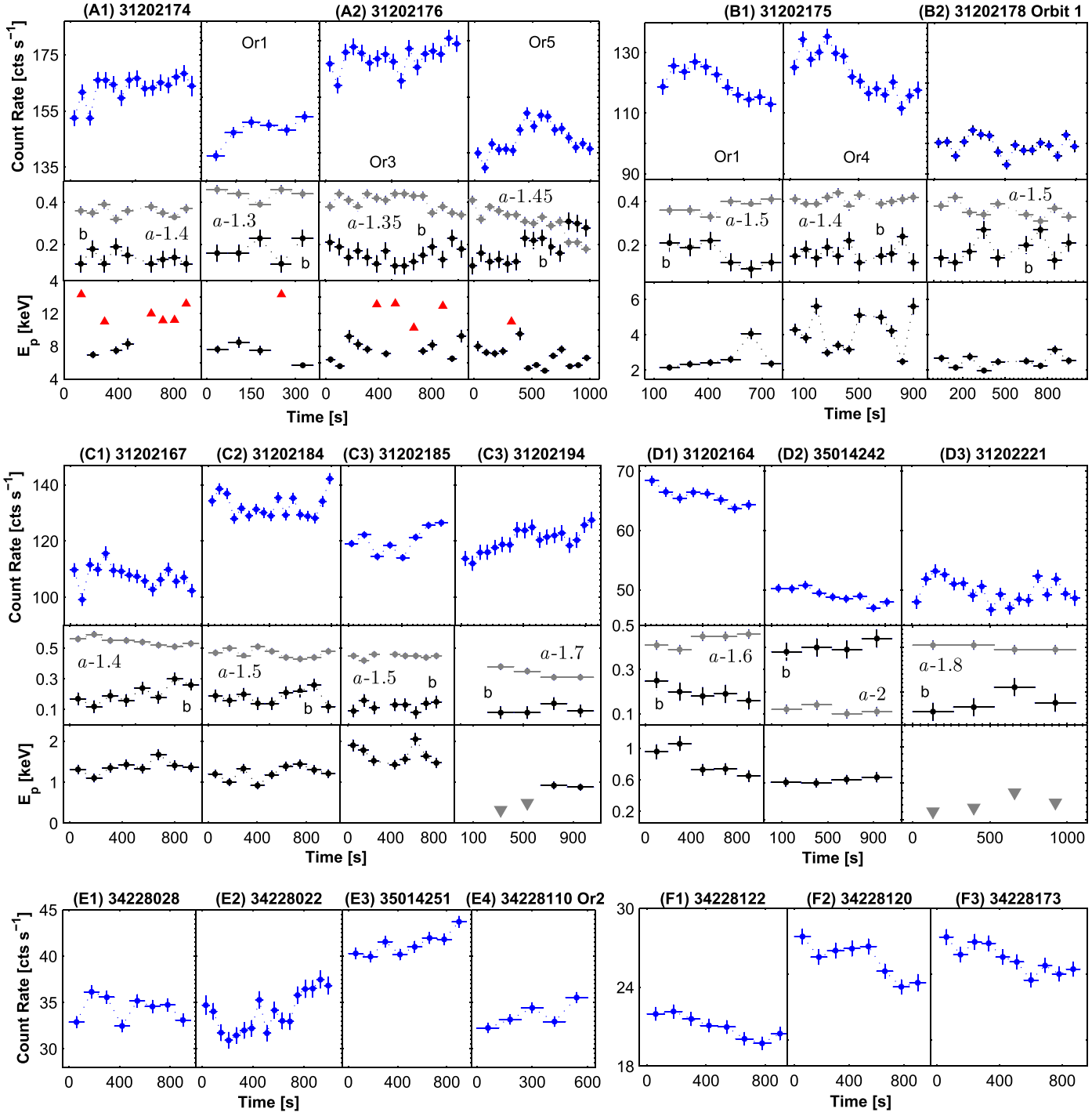

Figure 3. Fastest 0.3–10 keV IDVs. In the second panels of (A1)–(D3), the gray points correspond to the photon index *a*, arbitrarily shifted for better resolution. The red and gray triangles in the bottom panels of (A1)–(A2), (C3), and (D3) stand for the lower and upper limits to the intrinsic position of the synchrotron SED peak, respectively.

3. Results

3.1. X-Ray Variability

Table 2 provides a summary of the *Swift*-XRT and UVOT observations during 2015 December 8–2018 April 8. The source was targeted 299 times, with the net exposure time (sum of the good time intervals (GTIs)) of 314.5 ks. Based on the target's "visibility" for *Swift*, the observations were performed during 2015 December–2016 June, 2016 December–2017 June, and 2017 December–2018 April, denoted as interval 1, interval 2, and interval 3, respectively. Each interval was split into two subperiods (e.g., intervals 1a and 1b) according to the flaring activity of Mrk 421 in the *Swift*-XRT band.

The source was highly variable during intervals 1–3 (see Table 3 for the corresponding $F_{\rm var}$ and maximum-to-minimum flux ratios in different bands), although it showed significantly stronger X-ray flaring activity in interval 3 compared to the previous ones (Figure 1(a)): the mean 0.3–10 keV CR was a factor of ∼2–2.5 higher; during the 11 XRT pointings, the brightness exceeded a level of 100 counts s^{-1} (see Table 2),

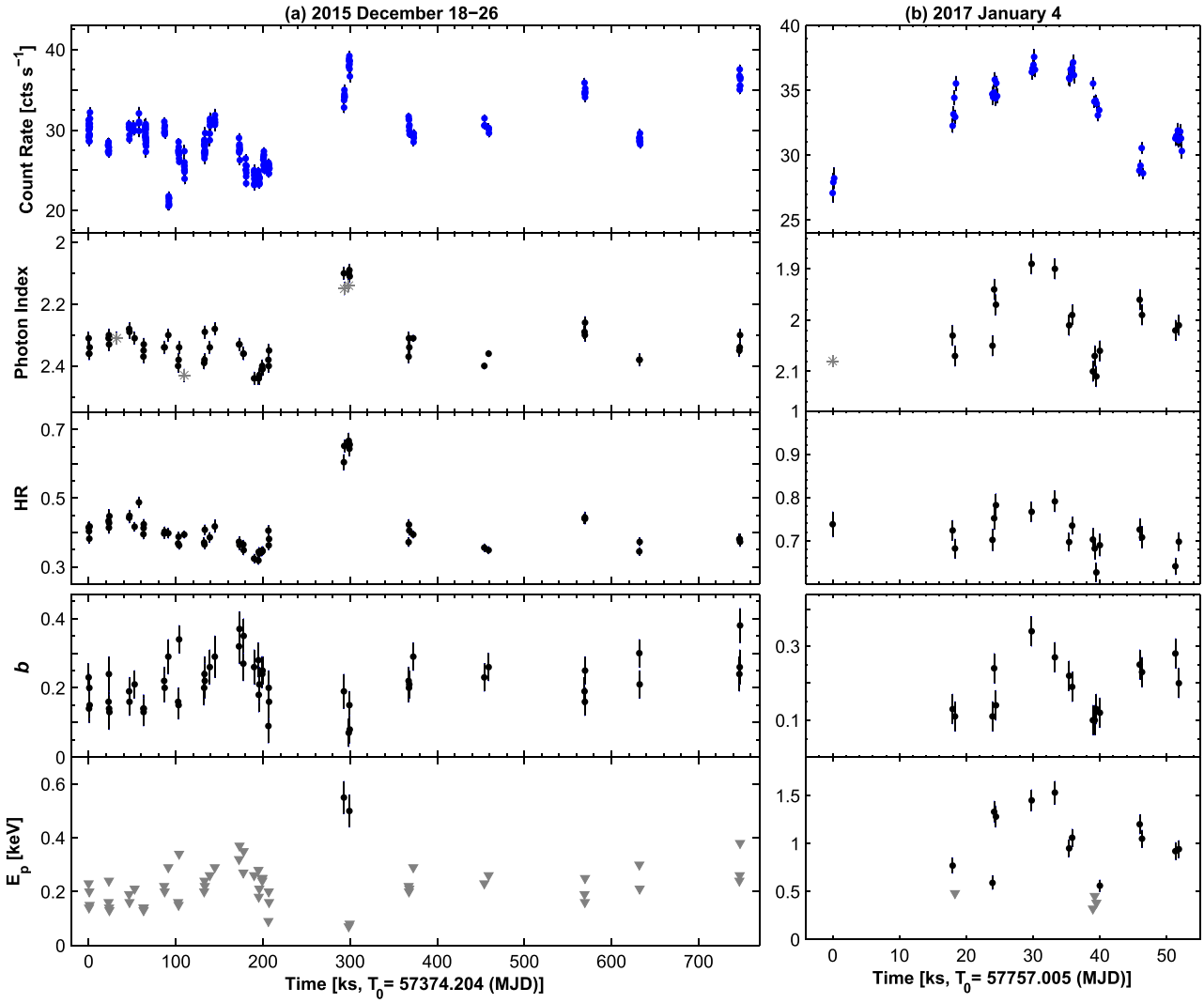

Figure 4. Two examples of the densely sampled 0.3–10 keV light curves with a weaker IDV. In the second panel, the black points and gray asterisks stand for the photon indices a and Γ, respectively. Gray triangles in the bottom panel stand for the upper limits to the intrinsic position of the synchrotron SED peak.

which was never recorded in intervals 1–2; and a generally higher state was superimposed by fast, strong flares by a factor of 2.2–3.8 (lasting 4–12 days) that were considerably fewer in the previous periods.

In interval 3, the most extreme flare occurred during 2018 January 14–30 with a 2 minute binned CR of 180.9 ± 2.8 counts s^{-1} (to the level observed on 2008 June 12; see Figure 1(b)), and the highest levels were recorded only during the giant X-ray outburst during 2013 April 10–17 (Kapanadze et al. 2016, 2018a). The source underwent fast brightness variations by 30%–45% within 13–35 ks during the declining phase of the flare (Figure 2, top panel). Note that the flux doubling time ($\tau_{\rm d} \approx 92$ ks, defined as $\tau_{\rm d} = \Delta t \times ln(2)/ln(F_2/F_1)$; Saito et al. 2013) was faster than the halving one ($\tau_{\rm d} \approx 113$ ks), and a similar situation was seen during the next flare, when an intraday flux doubling with $\tau_{\rm d} \approx 64$ ks was recorded (Figure 1(b)).

These events were preceded and followed by strong 0.3–10 keV flares by a factor of $\sim$2.5 and peak fluxes exceeding a level of 100 counts s^{-1} (Figures 1(c)–(c)). They were part of a well-defined long-term flare lasting more than 2 months (MJD 58,103–58,170). Other strong XRT-band flares are presented in Figures 1(f)–(i), with the intraday flux doubling/halving events within 4.8–18.9 hr. Among these flares, the 2015 December 29–2016 January 8 event was characterized by a two-peak maximum, possibly related to the propagation of forward and reverse shocks after the collision of two "blobs" in the blazar jet (see Böttcher & Dermer 2010).

The source also underwent extremely fast instances of the 0.3–10 keV intraday variability (IDV; brightness change within a day, detected by means of the χ^2 statistics; see Table 4 for details) at the 99.9% confidence level. Namely, the brightness showed a rise of 5%–18% (taking into account the associated measurement errors) in 180–600 s in Figures 3(A1) (panels (1)–(2)), (C2)–(C4), (D3), (E2), and (E3)–(E4). Figures 3(A)–(C) belong to the epoch of the strongest X-ray flaring activity in 2018 January 14–30. Note that the states with CR $\gtrsim$ 100 counts s^{-1} sometimes were associated with very fast and large drops just at the start of the XRT orbit that were related to instrumental effects. The source also showed very fast drops by 6%–16% within 180–840 s (Figures 3(B1), (C2), (D1)–(D3), (F1)–(F3)). Finally, entire brightness rising and dropping cycles with 6%–13% within 420–960 s were also observed (Figures 3(A2), (B2), (C1), (E1)). On the contrary, Mrk 421 sometimes showed a slow, low-amplitude variability during some densely sampled XRT observations in lower X-ray states

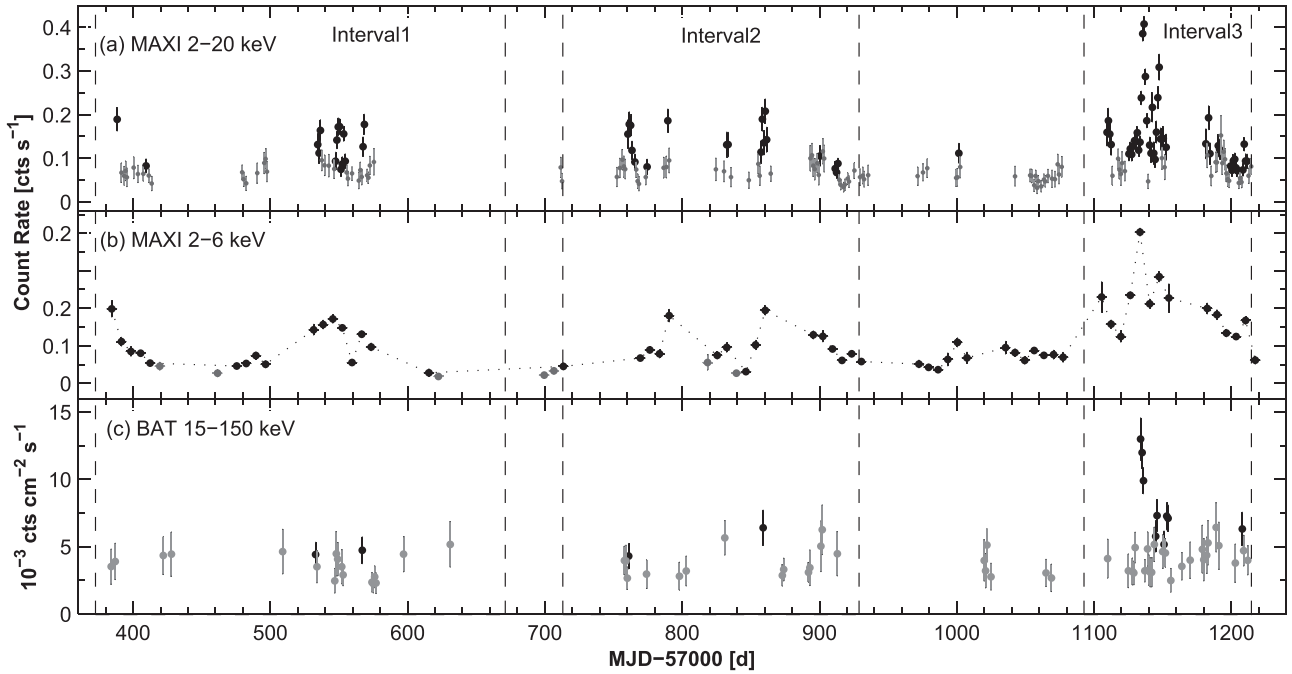

Figure 5. Long-term behavior of Mrk 421 in the MAXI 2–20 and 2–6 keV bands (panels (a) and (b), respectively), as well as in the BAT energy range (panel (c)). The daily binned data are used to construct light curves. The black and gray points correspond to the detections with 5σ and 3σ significances, respectively.

(see Figure 4). Moreover, tens of 0.3–10 keV IDVs were detected by us, and the details are reported in Table 4.

MAXI detected the source 78 and 61 times with 5σ significance in the 2–20 and 2–6 keV energy ranges, respectively (Figures 5(a)–(b)). Owing to lower instrumental capabilities, a strong long-term flare is evident only in interval 3. Significantly fewer detections with 5σ significance are found from the daily binned BAT data, which show a strong flare during the highest XRT and MAXI-band states (Figure 5(c)).

3.2. MWL Variability on Various Timescales

Similar to the XRT band, the strongest FACT VHE γ-ray flaring activity of Mrk 421 occurred in period 3a (Figure 6(a)). Namely, two strong flares peaking at MJD 58,111 and 58,135, as well as lower-amplitude ones with peaks at MJD 58,141, 58,145, and 58,164, accompanied the X-ray counterparts. The UVOT-band behavior was also predominantly correlated with the 0.3–10 keV flaring activity, while the source demonstrated different timing properties in the LAT band, showing slower variability and only one peak at the end of this subinterval, coinciding with the X-ray and VHE peaks.

The three subsequent peaks in the FACT-band light curve were evident during the strongest 0.3–10 keV activity of the source in interval 3b (Figure 6(b)). No LAT-band GTIs were obtained during the second half of this period, and a correlated behavior with X-ray variability was not observed in the first half. The optical–UV light curves showed a decline at the beginning of the subinterval, followed by the weak variability, which was not strongly correlated with the VHE–X-ray activity. However, a stronger correlation was observed during period 1a in the three consecutive peaks having X-ray and VHE counterparts (Figure 6(c)). Similarly, the LAT-band behavior was more correlated with those in the XRT and FACT bands, compared to that shown in interval 3.

The majority of interval 1b was also characterized by correlated X-ray and VHE flaring activity (Figure 6(d)). The peak days of the X-ray–VHE fluxes also coincided with enhanced activity of Mrk 421 in the LAT band. However, the source was not targeted with *Swift* and FACT during the strongest GeV-band flare peaking on MJD 57,441. Initially, the source was flaring at UV–optical frequencies (correlated with the higher-energy activity), while it showed a declining trend and low states afterward, during the four consecutive keV–TeV flares. A similar situation was observed in interval 2a when the source exhibited enhanced VHE and LAT-band activity during the long-term X-ray flare (see Figure 6(e)). Finally, Mrk 421 underwent strong VHE flares along with the X-ray ones in interval 2b, while the latter showed fewer correlations with the LAT and UVOT-band fluctuations (Figure 6(f)). The source did not show flares at the radio frequencies during any subinterval (see the bottom panels of Figure 6).

Although Mrk 421 frequently showed 8–16 detections a night with 3σ significance in the 20 minute binned FACT data (particularly in the time interval 2018 January–February), only three instances of a VHE IDV at the 99.9% confidence level were detected,[18] belonging to the epoch of the strongest X-ray flaring activity in the period presented here (see Figure 7(a) and Table 5). While no correlated X-ray–VHE variability was evident during MJD 58,136.1–58,136.3, the subsequent VHE data exhibit a brightness decline similar to the XRT ones. In the same period, the source showed one instance of an LAT-band IDV with a brightness decline by 42% (taking into account the associated errors) and accompanied by similar behavior in X-rays (Figure 7(b)). Finally, three ultraviolet IDVs, showing a brightness increase nearly simultaneous with that in the 0.3–10 keV energy range, are presented in Figures 7(c)–(d).

[18] Note that the FACT results are still provided in the form of the excess rates, and this result should be considered with caution.

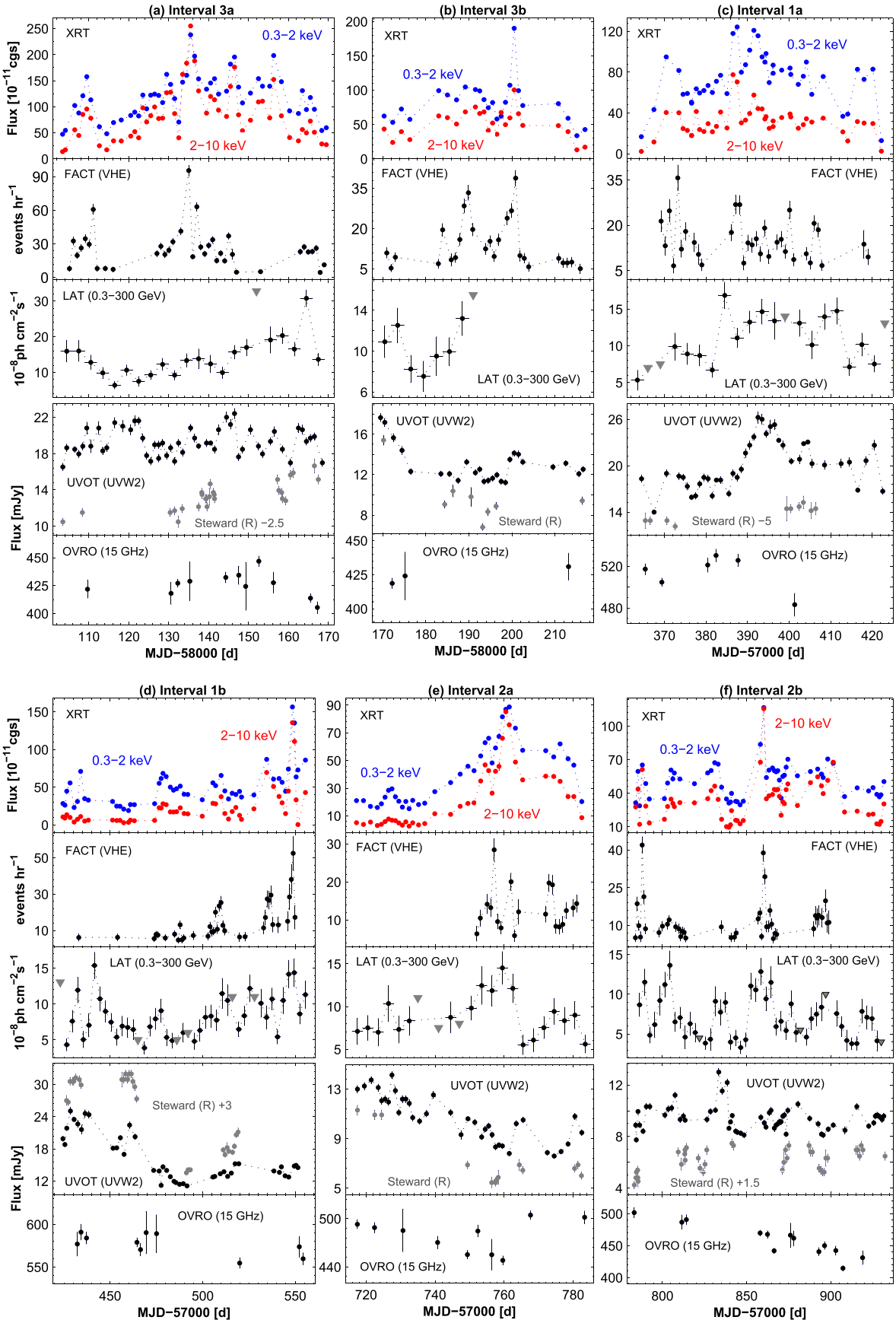

Figure 6. The MWL variability of Mrk 421 in different subintervals. The daily bins are used for the XRT, FACT, UVOT, Steward, and OVRO light curves, while 3 day bins are used for the LAT 0.3–300 GeV data. The triangles in the LAT-related plots stand for the 2σ upper limits to the 0.3–300 GeV flux when the source was detected below the 5σ significance and/or showing $N_{\rm pred} < 10$. The acronym "cgs" stands for erg cm^{-2} s^{-1}.

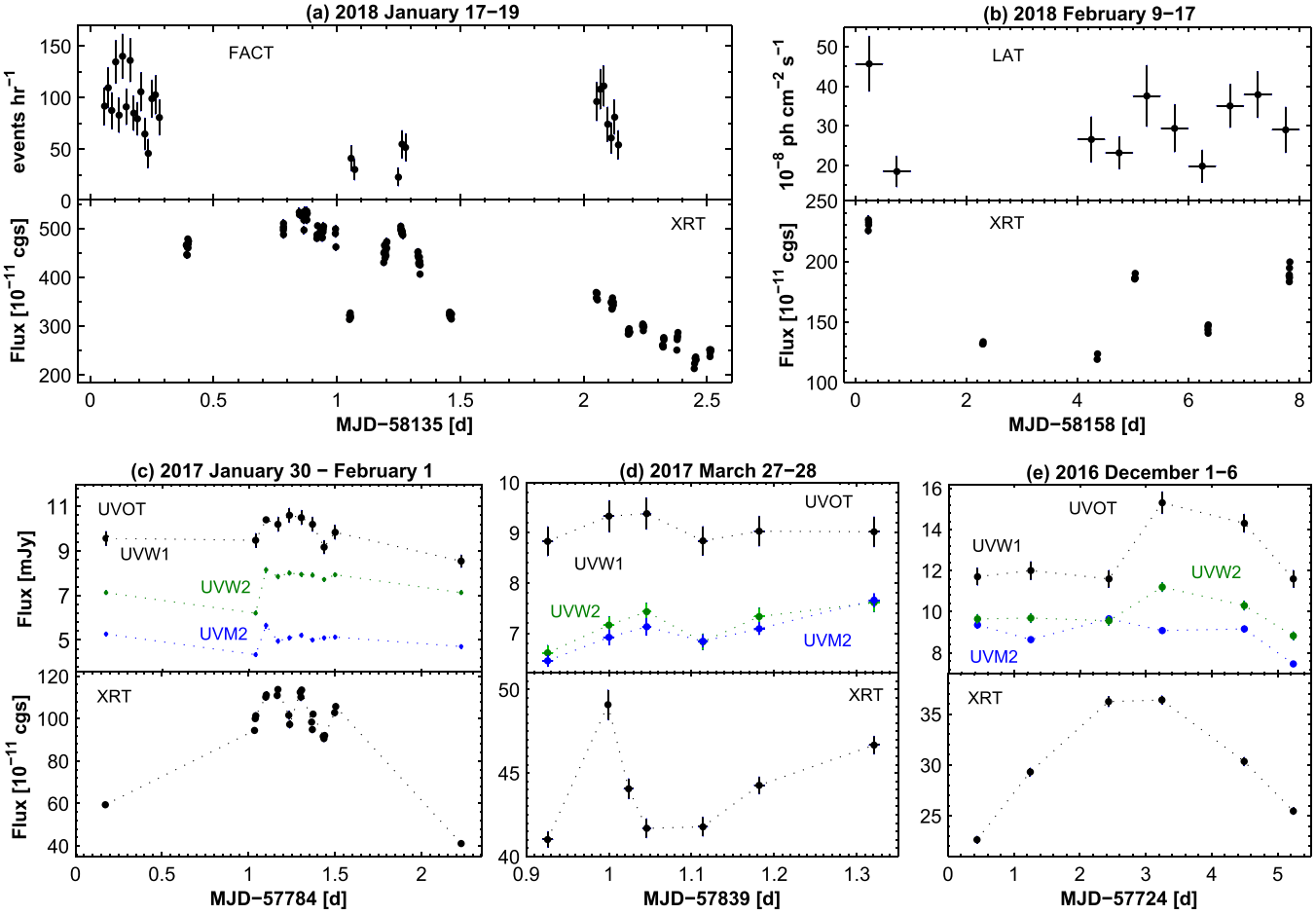

Figure 7. The IDV of Mrk 421 in the FACT (panel(a)), LAT (panel(b)), and UVOT (panels(c)–(e)) bands.

The details of another 35 optical–UV IDVs are provided in Table 5.

3.3. Spectral Variability

3.3.1. Curvature Parameter

Similar to the period 2005 March–2015 June (Kapanadze et al. 2016, 2017a, 2018a, 2018b), a vast majority of the 0.3–10 keV spectra of Mrk 421 (886 out of 980) show a significant curvature and are well fitted with the log-parabolic model. The corresponding results are presented in Table 6. The distribution of values of the curvature parameter b (corresponding to the curvature detection significance of 3σ and higher) for different periods is provided in Figures 8(A1)–(A4), and the corresponding properties (minimum, maximum, and mean values; distribution skewness) are listed in Table 7.

Figure 8(A1) demonstrates that the source was characterized by a relatively low curvature in the period 2015 December–2018 April: 98.1% of the values of the parameter b were smaller than $b = 0.4$ (conventional threshold between the lower and higher curvatures). Moreover, 46.2% of the spectra shows $b < 0.2$ (see Section 4.3 for the corresponding physical implication). The lowest curvatures were observed in interval 3: there were no spectra with $b > 0.4$, 62.3% of the values were lower than 0.2, and the mean value $\bar{b} = 0.18 \pm 0.01$ was significantly smaller than that recorded in interval 1 (see Table 7). The latter was characterized by the majority of the spectra showing curvatures with $b > 0.4$ (five out of nine, including the highest value for the entire 2.3 yr period presented here). Interval 2 was different from both cases and characterized by "intermediate" properties of the parameter b between intervals 1 and 3. This situation is clearly evident from the cumulative distributions of the curvature parameter presented in Figure 8(A3) and Table 8, providing the results of the K-S test and distances between the corresponding distributions.

According to Figure 8(A3) and Table 8, the distribution of parameter b shows differences between the different parts of intervals 2–3. The lowest curvatures are found for interval 3a ($\bar{b} = 0.17 \pm 0.01$, 66% of the spectra with $b < 0.2$, and $b_{\rm max}0.30 \pm 0.04$), while intervals 1a and 1b are not significantly different from each other.

The curvature parameter showed a weak positive correlation with the photon index at 1 keV and an anticorrelation with the position of the synchrotron SED peak, as observed in different subintervals (see Figures 9(a) and (b), as well as Table 9 for the corresponding values of the Spearman correlation coefficient ρ). Moreover, this parameter showed an anticorrelation with the de-absorbed 0.3–10 keV flux in intervals 1–2 (Figure 9(c)).

Column (6) of Table 4 demonstrates that the parameter b was variable 36 times at the 3σ confidence level during 0.3–10 keV IDVs, showing $\Delta b = 0.14(0.05)$–$0.31(0.06)$ within 0.38–23.92 hr (Figures 2–4). The fastest instances incorporated a curvature increase by 0.19(0.06)–0.22(0.06) in ∼1 ks (Figure 2 at

Table 5
The Optical–UV and γ-ray IDVs during 2015 December–2018 April

MJD (1)	Band (2)	ΔT (hr) (3)	χ^2/dof (4)	$100 \times F_{\rm var}$ (5)
57,380.79−57,381.56	*UVW2*	17.47	12.46/1	8.5(1.8)
57,391.56−57,392.21	*UVW1*	12.26	7.77/2	10.3(2.3)
57,425.25−57,426.23	*UVM2*	22.37	23.24/1	7.2(1.1)
57,426.18−57,426.49	*UVW2*	6.38	12.38/1	8.0(1.7)
57,430.17−57,430.35	*UVM2*	3.29	14.88/1	4.6(0.9)
57,477.97−57,478.21	*UVM2*	4.61	14.67/1	7.0(1.4)
57,477.97−57,478.21	*UVW2*	4.58	49.42/1	18.5(1.9)
57,724.44−57,725.29	*UVM2*	19.39	12.31/1	5.4(1.2)
57,726.44−57,727.29	*UVW1*	19.44	29.94/1	19.1(2.5)
57,726.44−57,727.29	*UVW2*	19.44	27.79/1	11.0(1.5)
57,728.49−57,729.28	*UVW1*	17.88	19.70/1	14.4(2.4)
57,728.49−57,729.28	*UVM2*	17.98	78.32/1	14.4(1.2)
57,728.49−57,729.28	*UVW2*	17.81	24.44/1	10.6(1.6)
57,755.22−57,756.20	*UVM2*	22.32	22.63/1	9.0(1.4)
57,784.17−57,785.08	*UVM2*	20.66	53.39/1	13.6(1.3)
57,784.17−57,785.08	*UVW2*	20.69	16.47/1	9.5(1.7)
57,785.03−57,785.54	*UVW1*	11.14	4.17/7	4.1(1.2)
57,785.03−57,785.54	*UVM2*	11.12	13.94/7	6.9(0.7)
57,785.03−57,785.54	*UVW2*	11.11	15.95/7	7.7(0.8)
57,785.37−57,786.27	*UVW1*	20.76	6.04/3	7.1(1.7)
57,785.37−57,786.27	*UVM2*	20.74	5.56/1	3.5(0.9)
57,785.37−57,786.27	*UVW2*	20.72	5.67/1	4.4(1.1)
57,839.93−57,840.37	*UVM2*	9.50	10.74/5	5.3(0.8)
57,839.93−57,840.37	*UVW2*	9.53	6.48/5	5.3(0.9)
57,843.91−57,844.41	*UVM2*	9.51	21.80/1	8.3(1.3)
57,873.87−57,874.12	*UVM2*	4.85	12.68/1	6.1(1.3)
57,873.87−57,874.12	*UVW2*	4.86	40.44/1	14.3(1.6)
57,926.42−57,927.40	*UVM2*	22.27	14.22/1	6.191.2)
58,103.44−58,104.34	*UVM2*	20.66	28.82/1	8.9(1.2)
58,103.44−58,104.34	*UVW2*	20.64	12.50/1	7.8(1.6)
58,112.36−58,113.35	*UVM2*	8.28	38.20/1	13.3(1.5)
58,123.91−58,124.48	*UVM2*	12.65	26.45/1	9.3(1.3)
58,123.91−58,124.48	*UVW2*	12.64	12.46/1	7.7(1.6)
58,137.05−58,137.55	*UVW1*	11.05	13.41/1	11.7(2.4)
58,146.68−58,147.32	*UVW1*	14.50	29.12/1	18.2(2.4)
58,146.68−58,147.32	*UVW2*	14.49	46.25/1	16.2(1.7)
58,147.217 −58,148.12	*UVM2*	19.03	14.88/1	6.2(1.2)
58,199.81−58,200.06	*UVW1*	4.73	19.56/1	13.5(2.2)
58,139.60−58,140.40	*V*	19.20	14.19/2	7.2(1.7)
58,139.60−58,140.40	*R*	19.21	7.59/2	7.2(2.2)
58,158.00−58,158.98	0.3−300 GeV	23.52	11.62/1	57.6(12.8)
58,135.059 −58,136.058	VHE	23.58	2.82/16	23.4(5.4)
58,135.236 −56,136.073	VHE	20.09	4.44/5	41.1(10.1)
58,136.250 −58,137.141	VHE	21.38	4.22/9	32.3(7.8)

MJD 58,135.93; Figure 4 at MJD 57,375.4). Moreover, the curvature parameter varied with 2σ and 1σ significances (capable of causing a significant flux change) 43 and 22 times, respectively.

3.3.2. Photon Index and HR

Although the photon index at 1 keV showed a very wide range of values ($\Delta a = 1.29$) with the hardest spectrum yielding $a = 1.63 \pm 0.02$ in the period presented here, this range is narrower compared to that recorded in the time interval 2009–2012 ($\Delta a = 1.51$). In the latter, the source showed the hardest ($a = 1.51$–1.61) and softest ($a = 2.93$–3.02) spectra since the start of the *Swift* operations. On the other hand, narrower ranges were found in the time intervals 2005–2008, 2013 April, and 2013 November–2015 June (1.01, 0.87, and 0.94, respectively).

Similar to the previous periods, the source clearly demonstrated a "harder-when-brighter" spectral behavior during the 0.3–10 keV flares. Figure 9(d) exhibits a strong anticorrelation between the parameter a and the de-absorbed 0.3–10 keV flux (see also Table 9). This trend was evident in intervals 1–3 and subintervals separately, although with different strengths and slopes of the corresponding scatter plot. Moreover, Figure 10(b) shows some short time intervals when the opposite spectral trend was observed (during MJD 57,370.42–57,374.47, 57,426.45–57,428.31, etc.).

There were 294 spectra harder than $a = 2$ (conventional threshold between the hard and soft X-ray spectra), amounting to 33.2% of all log-parabolic spectra (see Figure 8(B1)). Note that this percentage is smaller than in the periods 2005–2008, 2009–2012, and 2013 January–May (39%–46%) and higher than those shown in 2013 November–2015 June (20%; see Kapanadze et al. 2016, 2017a, 2018a, 2018b). On average, the hardest spectra with the mean value $\overline{a} = 1.98 \pm 0.01$ were observed in interval 3a versus the softest spectra belonging to interval 1 ($\overline{a} = 2.29 \pm 0.01$). Figures 8(B2)–(B5) and Table 8 clearly show that the distribution properties of parameter a varied not only from interval to interval but also among the subintervals.

Similar to the curvature parameter b, the photon index a showed an extreme variability on diverse timescales. It varied at the 3σ confidence level 69 times with $\Delta a = 0.08(0.03)$–$0.31(0.02)$ within 0.27–23.97 hr along with the X-ray IDVs (see col. (5) of Table 4 and Figures 2–4). Among them, five subhour instances were recorded: hardenings by $\Delta a = 0.08(0.03)$–$0.23(0.03)$ within 0.13–0.28 hr. On longer timescales, the largest variabilities with $\Delta a = 0.66$–1.07 in 3.1–27.6 days were observed along with the strong 0.3–10 keV flares (Figure 10(b)).

The HRs, derived from the log-parabolic and power-law spectra (see Table 10), showed a wide range of values (ΔHR = 1.09), with 68.7% of the spectra with HR > 0.5 and 90 spectra (9.2%) showing HR > 1 (see Figure 8(D1) and Table 7) when the de-absorbed 2–10 keV flux is higher than the 0.3–2 keV one. A vast majority of the latter (90%) belong to interval 3a, characterized by the highest mean value $\overline{\rm HR} = 0.79 \pm 0.01$ (versus $\overline{\rm HR} = 0.42$–0.65 in other subintervals; Figures 8(D2)–(D3)). A positive $F_{0.3-10\rm keV}$–HR correlation was observed in all intervals, demonstrating a dominance of the "harder-when-brighter" spectral evolution during X-ray flares, although this trend was significantly weaker in interval 1 (see Figure 9(f) and Table 9). The long-term behavior of the HR followed that of parameter a: during the largest variability of the photon index, HR increased by a factor of 3.5–6.4 and showed 75 IDVs by 11%–88% (see col. (8) of Table 4).

3.3.3. The Position of the Synchrotron SED Peak

During the period 2015 December–2018 April, 463 spectra (52.3% of those showing a curvature) are characterized by 0.5 keV $\leqslant E_{\rm p} \leqslant$ 8 keV when the position of the synchrotron SED peak is well constrained by the XRT data (see Kapanadze et al. 2018b). In the case of 407 spectra (46%), $E_{\rm p} < 0.5$ keV when the synchrotron SED peak position, derived via the X-ray spectral analysis, should be assumed as an upper limit to the

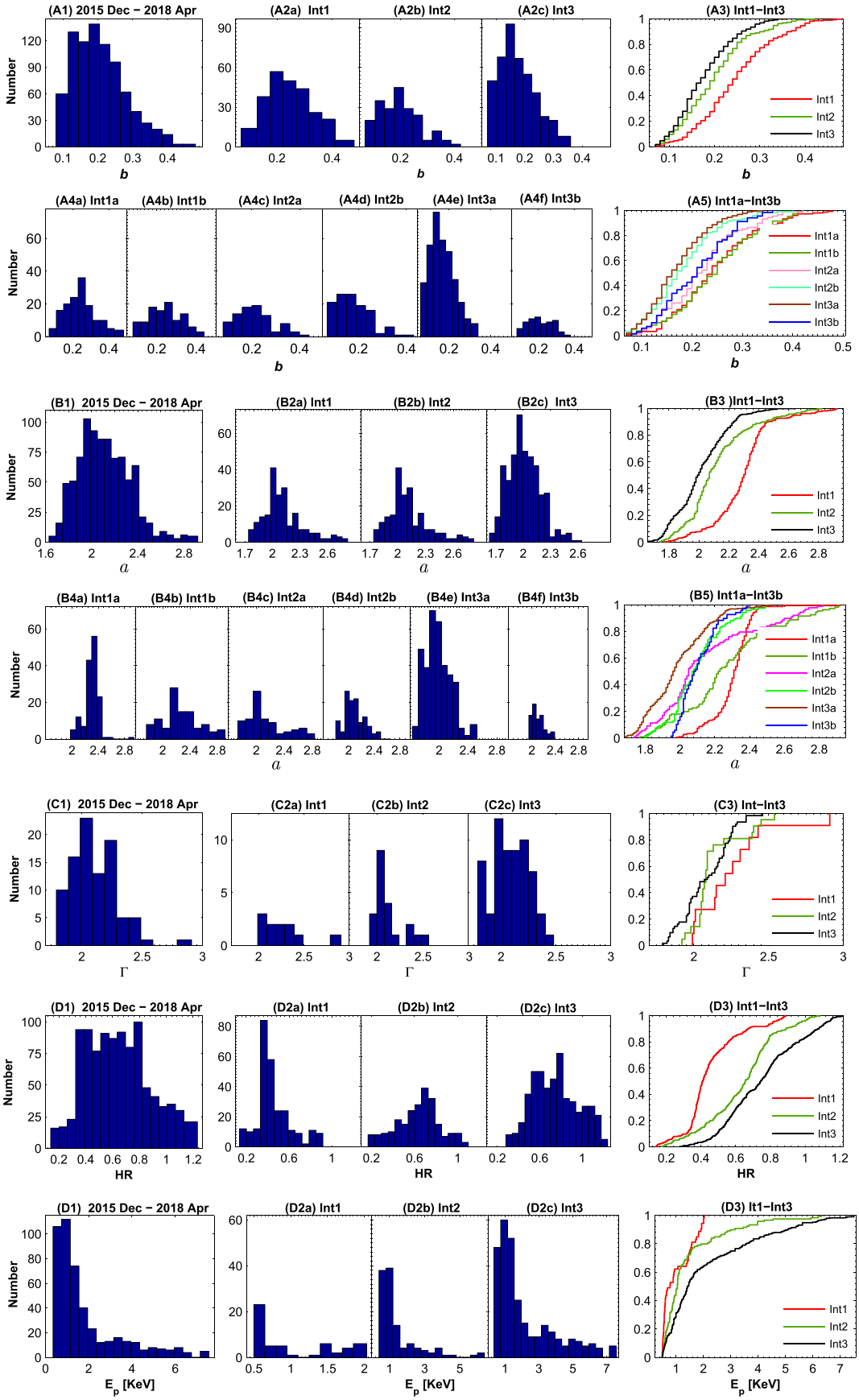

Figure 8. Distribution of the spectral parameter values in different periods: histograms and the corresponding normalized cumulative distributions (last plot in each row).

Table 6
The Results of the *Swift*-XRT Spectral Analysis with the Log-parabolic Model

ObsId (1)	a (2)	b (3)	E_p (4)	$10 \times K$ (5)	χ^2/dof (6)	$F_{0.3-2\ keV}$ (7)	$F_{2-10\ keV}$ (8)	$F_{0.3-10\ keV}$ (9)	HR (10)
35014240	2.92(0.02)	0.27(0.08)	0.02(0.01)	0.41(0.01)	1.04/145	16.71(0.27)	2.34(0.14)	19.05(0.35)	0.14(0.01)
35014241	2.49(0.01)	0.48(0.04)	0.31(0.05)	1.31(0.01)	1.10/244	43.35(0.40)	11.59(0.32)	54.95(0.50)	0.27(0.01)
35014242 S1(267 s)	2.22(0.02)	0.38(0.04)	0.51(0.06)	3.12(0.04)	1.07/230	94.62(1.08)	40.46(1.19)	135.21(1.55)	0.43(0.01)
35014242 S2(267 s)	2.24(0.02)	0.40(0.04)	0.50(0.06)	3.19(0.04)	1.00/236	97.05(1.11)	39.90(1.18)	136.77(1.57)	0.41(0.01)

Note. See the corresponding machine-readable table for the full version. Col. (1): ObsID of the particular observation, along with the duration of the separate segments (in seconds) used to extract a spectrum in parentheses. The abbreviations "or" and "s" stand for "orbit" and "segment," respectively. Cols. (2)–(3): values of the photon index at 1 keV and the curvature parameter, respectively. Col. 4: E_p values in keV. Cols. 5 and 6: norm and χ^2, respectively. Cols. (7)–(9): de-absorbed 0.3–2, 2–10, and 0.3–10 keV fluxes in erg cm^{-2} s^{-1}. Col. (10): HR.

(This table is available in its entirety in machine-readable form.)

intrinsic peak position (not used by us for the construction of the scatter plots and distributions). Note that such instances amounted to 86.6% and 68.9% of all curved spectra from intervals 1a and 1b, respectively (versus 25.4% in interval 3a). Moreover, the majority of the spectra with $E_p < 0.1$ keV (when the synchrotron SED peak is situated in the UV energy range) belonged to these subintervals.

On the other hand, for the spectra with $E_p > 8$ keV, the synchrotron SED peak is poorly constrained by the observational data, and such E_p values should be considered as lower limits to the intrinsic position (see Kapanadze et al. 2018b). During the period 2015 December–2018 April, the source showed 14 spectra with 8.25 keV $\leqslant E_p \leqslant$ 15.85 keV, mostly from the observations corresponding to the highest X-ray states in interval 3a.

The E_p values from the range 0.5–8 keV mainly belong to interval 3 (62.9%), and their mean is significantly higher than those from intervals 1–2 (2.16 keV versus 1.02–1.46 keV in intervals 1–2; see Figure 8(D2) and Table 7). Note that the K-S test and related Monte Carlo simulations did not show a significant difference between the distributions corresponding to intervals 1 and 2 (see Table 8). For the entire 2015 December–2018 April period, the parameter E_p showed a positive correlation with $F_{0.3-10keV}$, which was the strongest in interval 3 (Figure 9(g) and Table 9). Moreover, a positive correlation between E_p and S_p (the height of the synchrotron SED peak) was detected in all three time intervals (see Figure 9(h), Table 9, and Section 4.3 for the corresponding physical implication). Note that the latter quantity was calculated for each spectrum as (Massaro et al. 2004)

$$S_p = 1.6 \times 10^{-9} K 10^{(2-a)^2/4b}\ \mathrm{erg\ cm^{-2}\ s^{-1}}. \quad (6)$$

On intraday timescales, the parameter E_p varied 56 times at the 3σ confidence level, observed during the 0.3–10 keV IDVs (see col. (7) of Table 4). The most dramatic changes were observed during the extreme flare in 2018 January 14–30 (see the bottom panels of Figures 2 and 3(A1)–(A2)): E_p sometimes showed shifts by several keV within 0.1–9.5 hr to higher energies and moved back in comparable timescales.

4. Conclusions and Discussion

4.1. X-Ray and MWL Flux Variability

4.1.1. Variability Character

The 0.3–10 keV brightness of the source reached the highest level in the time interval 2018 January–February, and Mrk 421 was brighter only during the giant outburst in 2013 April. A similar situation was observed in the VHE range: the highest VHE states were recorded in 2018 January (coinciding with those in the XRT band), while the strongest VHE flare was observed in 2013 April. The TeV-band variability mostly showed a good correlation with the X-ray one, although there were some exceptions (see Figure 6 and Section 4.2). Conversely, there were significantly fewer detections with 5σ significance and/or lower fluxes in the BAT band compared to the periods 2005 December–July, 2008 March–July, 2009 October–November, 2010 January–May, and 2011 September (see a more detailed discussion in Section 4.3.5).

In other spectral ranges, Mrk 421 exhibited a relatively different behavior. Namely, the highest 0.3–300 GeV flux from the weekly binned LAT data was $(2.2 \pm 1.8) \times 10^{-7}$ ph cm^{-2} cm^{-1} (in 2016 February, not coinciding with the highest X-ray states). Contrary to the X-ray and VHE observations, significantly higher levels were recorded in 2012 July–August (with the highest historical MeV–GeV level) and the comparable states in 2013 March and 2014 April. There was a frequent absence or weakness of the correlation between the LAT-band and X-ray variability (Kapanadze et al. 2016, 2017a).

In the *UVW1–UVW2* bands, the highest states, corresponding to the dereddened and host-subtracted fluxes of 23.3–29.8 mJy, were observed during 2016 January–February, and they were significantly lower 2 yr later when the source showed its highest X-ray activity. The higher UV states were observed in 2010 June–2011 April, 2012 April–May, 2012 December–2013 April (the highest historical UV brightness, preceding the giant X-ray outburst), 2013 November–2014 April, and 2015 February–June. A similar situation was found in the optical *V–R* and OVRO bands.

We checked the MWL data of Mrk 421 for periodicity during 2015 December–2018 April. As an example, Figure 11 presents the LSP and WWZ plots from the XRT observations performed in intervals 1–3. No clearly expressed quasi-periodic variations are found in this energy range, similar to the radio–UV and GeV–TeV ranges. Periodic brightness variations have also not been found by different authors (see, e.g., Carnerero et al. 2017; Sandrinelli et al. 2017).

As in past years, the source showed a double-humped behavior in the plane $\log \nu$–F_{var} during the entire 2015 December–2018 April period and its separate intervals (with F_{var} calculated using the entire data set obtained in the given spectral band during the particular period; see Figures 12(A1)–(A4) and Kapanadze et al. 2016, 2017a, 2018a, 2018b). We used the 1 day binned XRT, BAT, FACT, OVRO, and optical–UV data in our study,

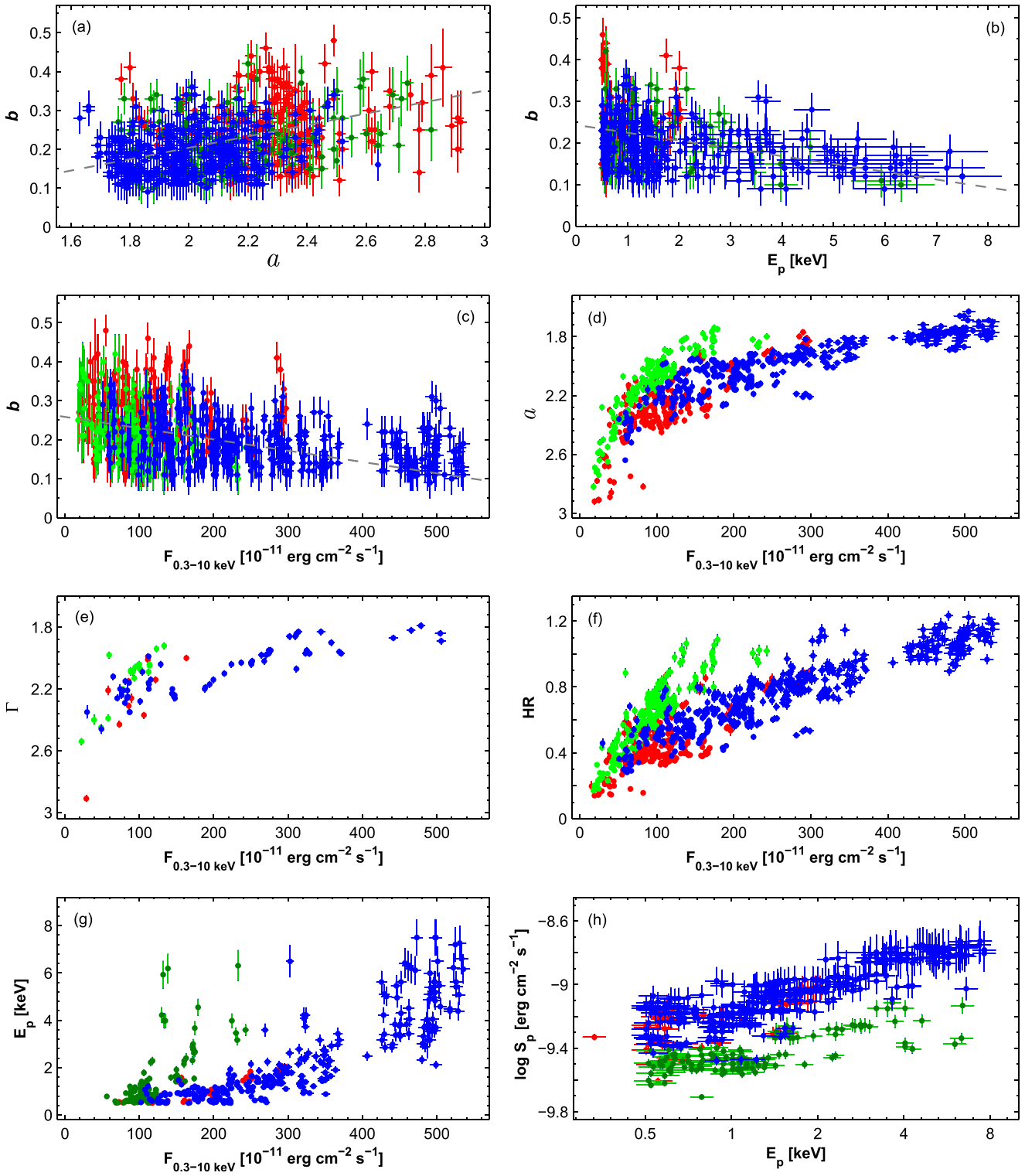

Figure 9. Correlation between the spectral parameters and de-absorbed 0.3–10 keV flux. Panels (a)–(c): curvature parameter b plotted vs. photon index a, position of the synchrotron SED peak E_p, and de-absorbed 0.3–10 keV flux, respectively. The parameters a, Γ, HR, and E_p are plotted vs. the de-absorbed 0.3–10 keV flux in panels (d)–(g). The scatter plot E_p–logS_p is provided in panel (h). The colored points correspond to the different intervals as follows: red—interval 1; green—interval 2; blue—interval 3. Gray dashed lines represent linear fits to the scatter plots.

while the 3 day binned LAT was used in the 0.3–300 GeV energy range (similar to the light curves provided in Figure 6). Although the latter binning and the cuts at 3σ–5σ detection significances can lead to some undersampling in the corresponding F_{var} values, a two-humped shape with the synchrotron and higher-energy peaks situated at the X-ray and VHE frequencies, respectively, seems to be inherent for HBLs and is frequently reported for these sources. For our target, a similar result was reported by various authors from various MWL campaigns (Alecsic et al. 2015a, 2015b; Ahnen et al. 2016; Abeysekara et al. 2017), favoring the one-zone SSC model (predicting the correlated X-ray–VHE variability) for Mrk 421 in different shorter-term periods and indicating that the

Table 7
Distribution of Spectral Parameters in Different Periods

Par. (1)	Min. (2)	Max. (3)	Mean (4)	Skewness (5)
		2015–2018		
b	0.07(0.04)	0.48(0.04)	0.20(0.01)	0.66
a	1.63(0.02)	2.92(0.02)	2.12(0.01)	0.58
Γ	1.79(0.02)	2.91(0.02)	2.12(0.02)	0.98
HR	0.14(0.01)	1.23(0.03)	0.64(0.01)	0.28
$E_{\rm p}$	0.50(0.06)	7.50(0.76)	1.85(0.09)	1.65
		Int1		
b	0.07(0.04)	0.48(0.04)	0.25(0.01)	0.34
a	1.77(0.02)	2.92(0.02)	2.29(0.01)	0.31
Γ	1.99(0.02)	2.91(0.02)	2.12(0.04)	1.37
HR	0.14(0.01)	0.89(0.03)	0.45(0.01)	0.91
$E_{\rm p}$	0.50(0.06)	2.03(0.14)	1.02(0.18)	0.94
		Int1a		
b	0.09(0.04)	0.48(0.04)	0.25(0.01)	0.61
a	1.98(0.02)	2.92(0.02)	2.30(0.01)	−0.37
HR	0.14(0.01)	0.68(0.02)	0.42(0.01)	0.98
		Int1b		
b	0.08(0.04)	0.42(0.05)	0.25(0.01)	0.25
a	1.77(0.02)	2.91(0.02)	2.26(0.01)	0.41
HR	0.14(0.01)	0.89(0.03)	0.49(0.01)	0.33
		Int2		
b	0.07(0.04)	0.42(0.05)	0.20(0.01)	0.58
a	1.74(0.02)	2.82(0.02)	2.12(0.01)	1.02
Γ	1.92(0.02)	2.54(0.02)	2.13(0.03)	1.22
HR	0.17(0.01)	1.09(0.03)	0.63(0.01)	−0.20
$E_{\rm p}$	0.51(0.06)	6.31(0.65)	1.46(0.22)	2.17
		Int2a		
b	0.10(0.04)	0.40(0.04)	0.22(0.01)	0.48
a	1.74(0.02)	2.82(0.02)	2.14(0.01)	0.84
HR	0.17(0.01)	1.09(0.03)	0.61(0.01)	−0.23
		Int2b		
b	0.07(0.04)	0.40(0.04)	0.18(0.01)	0.12
a	1.80(0.02)	2.50(0.02)	2.10(0.01)	0.47
HR	0.29(0.01)	1.06(0.04)	0.65(0.01)	0.14
		Int3		
b	0.07(0.04)	0.36(0.04)	0.18(0.01)	0.53
a	1.63(0.02)	2.64(0.01)	2.01(0.01)	0.43
Γ	1.79(0.02)	2.60(0.02)	2.08(0.02)	0.05
HR	0.28(0.01)	1.23(0.03)	0.75(0.01)	0.19
$E_{\rm p}$	0.50	7.50(0.76)	2.16(0.17)	1.30
		Int3a		
b	0.07(0.04)	0.30(0.04)	0.17(0.01)	0.34
a	1.63(0.02)	2.52(0.02)	1.98(0.01)	0.54
HR	0.28(0.01)	1.23(0.03)	0.79(0.01)	−0.04
		Int3b		
b	0.08(0.04)	0.36(0.04)	0.21(0.01)	0.16
a	1.95(0.02)	2.39(0.02)	2.11(0.01)	0.78
HR	0.36(0.02)	0.80(0.03)	0.60(0.01)	−0.19

Note. Minimum and maximum values (Cols (2) and (3), respectively), mean value (Col. (4)) and skewness (last column).

electron energy distribution is most variable at the highest energies (Alecsic et al. 2015b).

Although the optical data points in Figures 12(A1)–(A2) violate the general trend of increasing variability power from radio to hard X-ray frequencies, this result can be related to the data sampling: some *V*- and *R*-band observations were carried out at Arizona Observatory in those time intervals when the source was not targeted by UVOT, although it was showing a strong variability. The presence of lower VHE peaks in Figures 12(A1)–(A3), compared to the peak in the synchrotron frequency, is difficult to explain via the upscattering of synchrotron photons in the Thomson regime (when a squared relation is expected). However, this result can be related to the use of the FACT excess rates instead of the linear fluxes in our study.

4.1.2. Flux Lognormality

We also checked whether the X-ray and MWL fluxes of Mrk 421 observed in the 2015 December–2018 April time interval showed lognormal distributions. According to McHardy (2008), a lognormal flux behavior in blazars can be indicative of the variability imprint of the AD onto the jet. Moreover, the lognormal fluxes have fluctuations that are, on average, proportional to the flux itself and indicative of an underlying multiplicative, rather than additive, physical process. Consequently, the excess variance $\sigma^2_{\rm excess} = \sqrt{S^2 - \overline{\sigma_{\rm err}}^2}$ (with the quantities S and $\overline{\sigma^2_{\rm err}}$ defined in Equation (3)) plotted versus the mean flux for all flares should show an increasing linear trend (Chevalier et al. 2019).

For BLLs, the lognormality in different spectral ranges and time intervals was reported for PKS 2155–304, BL Lac, and 1ES 1011+496 (Giebels & Degrange 2009; Sinha et al. 2017; Chevalier et al. 2019). In the case of Mrk 421, the lognormality was studied by Sinha et al. (2017) using the radio, optical–UV, and LAT-band data obtained during 2009–2015. The lognormal fit to the histograms was clearly preferred for most of the bands, leading to the suggestion that the flux variability in the source can be mainly attributed to changes in the particle spectrum rather than to the variability of the jet physical parameters, such as the magnetic field or Doppler factor (see Sinha et al. 2016).

In order to investigate lognormality, we fit the histograms of the MWL fluxes with the Gaussian and lognormal functions (similar to the aforementioned studies). Figure 13(A1) demonstrates that the distribution of the de-absorbed 0.3–10 keV flux from the entire 2015 December–2018 April period is closer to the lognormal shape than the Gaussian one (similar to the MAXI observations; Figure 13(B)). A lognormal behavior is confirmed by the corresponding scatter plot in the $\sigma^2_{\rm excess}$–$\overline{F_{0.3-10\ {\rm keV}}}$ plane, where the data points, corresponding to the XRT-band flares during 2015 December–2018 April, show an increasing linear trend with higher mean flux (Figure 13(H1)). Note that this result is mainly due to the observations performed in intervals 1 and 3, while the data from interval 2 are closer to the Gaussian function (Figures 13(A2)–(A6)).

The longer-term flares may result from the propagation and evolution of relativistic shocks through the jet (see Sokolov et al. 2004 and references therein). The shock appearance can be related to the instabilities occurring in the AD, which may momentarily saturate the jet with extremely energetic plasma

Table 8
Results from the K-S Test

	K-S						$D_{K\text{-}S}$					
Quant. (1)	Int1–Int2 (2)	Int1–Int3 (3)	Int2–Int3 (4)	Int1a–Int1b (5)	Int2a–Int2b (6)	Int3a–Int3b (7)	Int1–Int2 (8)	Int1–Int3 (9)	Int2–Int3 (10)	Int1a–Int1b (11)	Int2a–Int2b (12)	Int3a–Int3b (13)
b	1	1	1	0	1	1	0.25	0.38	0.15	⋯	0.34	0.27
a	1	1	1	1	1	1	0.49	0.61	0.26	0.32	0.19	0.47
Γ	0	0	0	⋯	⋯	⋯	⋯	⋯	⋯	⋯	⋯	⋯
HR	1	1	1	1	0	1	0.50	0.62	0.25	0.31	⋯	0.55
E_p	0	1	1	⋯	⋯	⋯	⋯	0.37	0.28	⋯	⋯	⋯

Note. In cols. (2)–(7), 1 indicates that data sets are different from each other, and the corresponding distance between the normalized cumulative distributions are provided in cols. (8)–(13); 0 indicates no significant difference between the data sets.

Table 9
Correlations between Spectral Parameters and 0.3–10 keV Flux in Different Periods

Quantities	ρ	p
2015 Dec–2018 Apr		
a and b	0.33(0.08)	6.23×10^{-6}
b and E_p	−0.34(0.09)	1.04×10^{-6}
b and $F_{0.3-10\ keV}$	−0.33(0.10)	3.42×10^{-6}
a and $F_{0.3-10\ keV}$	−0.80(0.03)	3.08×10^{-14}
Γ and $F_{0.3-10\ keV}$	−0.75(0.07)	7.42×10^{-13}
HR and $F_{0.3-10\ keV}$	0.79(0.04)	4.19×10^{-14}
E_p and $F_{0.3-10\ keV}$	0.69(0.08)	4.34×10^{-12}
log E_p and log S_p	0.65(0.08)	3.39×10^{-11}
$\Gamma_{0.3-2\ GeV}$ and $\Gamma_{2-300\ GeV}$	0.39(0.09)	1.99×10^{-8}
Int1		
a and b	0.29(0.09)	1.00×10^{-5}
a and $F_{0.3-10\ keV}$	−0.70(0.04)	6.56×10^{-12}
Γ and $F_{0.3-10\ keV}$	−0.73(0.907)	3.04×10^{-6}
HR and $F_{0.3-10\ keV}$	0.64(0.06)	1.24×10^{-10}
E_p and $F_{0.3-10\ keV}$	0.73(0.08)	2.51×10^{-10}
log E_p and log S_p	0.64(0.07)	8.99×10^{-10}
Int2		
a and b	0.23(0.08)	3.34×10^{-4}
b and E_p	−0.30(0.10)	8.60×10^{-5}
b and $F_{0.3-10\ keV}$	−0.31(0.10)	9.11×10^{-6}
a and $F_{0.3-10\ keV}$	−0.88(0.03)	$<10^{-15}$
Γ and $F_{0.3-10\ keV}$	−0.70(0.10)	7.66×10^{-5}
HR and $F_{0.3-10\ keV}$	0.88(0.03)	$<10^{-15}$
E_p and $F_{0.3-10\ keV}$	0.69(0.09)	7.15×10^{-9}
log E_p and log S_p	0.62(0.07)	6.02×10^{-10}
Int3		
a and b	0.32(0.08)	6.23×10^{-12}
b and E_p	−0.32(0.09)	4.48×10^{-5}
b and $F_{0.3-10\ keV}$	−0.30(0.11)	8.19×10^{-5}
a and $F_{0.3-10\ keV}$	−0.86(0.03)	1.03×10^{-15}
Γ and $F_{0.3-10\ keV}$	−0.85(0.05)	2.47×10^{-14}
HR and $F_{0.3-10\ keV}$	0.89(0.03)	$<10^{-15}$
E_p and $F_{0.3-10\ keV}$	0.85(0.06)	1.69×10^{-14}
log E_p and log S_p	0.83(0.05)	5.54×10^{-14}

Note. In cols. (2)–(3), ρ and p stand for the Spearman coefficient and corresponding p-chance, respectively.

with much higher pressure than the steady jet plasma downstream (Sokolov et al. 2004). Consequently, a lognormal flaring activity of the source on longer timescales may indicate a variability imprint of the AD onto the jet. However, the fluxes, corresponding to the highest X-ray states in intervals 1 and 3, produce outliers from the lognormal distributions. These states generally were recorded during fast flares superimposed on the long-term one. These flares could be triggered by the shock interaction with the jet inhomogeneities whose origin was related to the jet instabilities (e.g., strong turbulent structures; Marscher 2014). Therefore, no lognormal distribution of those fluxes is expected in that case, owing to the absence of the AD variability imprint. Moreover, interval 2 clearly shows a better fit to the Gaussian function, and since this period was characterized, on average, by lower X-ray states (see Section 3.1 and Table 3), this result could be related to the propagation of weaker shocks through the jet. On the other hand, a shock weakness possibly was due to the lower AD variability in that period, which resulted in a lesser imprint onto the jet of Mrk 421.

In each interval, the FACT and LAT-band fluxes clearly showed a better fit of the lognormal function with the corresponding distributions (Figures 13(C1)–(D4)). Although the same is shown by the R-band histogram constructed for the entire 2015 December–2018 April period, it is impossible to draw a firm conclusion related to the lognormal behavior of the source in this band, since we could not construct the corresponding $\overline{F_R}$–σ^2_{excess} scatter plot due to the sparse sampling of the optical flares (see Figure 6). In contrast, the OVRO data do not show a good fit between the corresponding histogram and lognormal function. This result implies radio contributions from various emission regions with different physical conditions. Finally, the UVOT-band histograms show a better (but not good) fit with the lognormal function compared to the Gaussian one only in interval 2 (see the bottom row of Figure 13).

4.1.3. IDV

In the 2015 December–2018 April period, the source showed three intraday flux doubling and three flux halving events with $\tau_d = 14.2$–17.8 hr and $\tau_h = 4.8$–18.9 hr, respectively. Note that the flux doubling time can be used for constraining the upper limit to the emission zone as (Saito et al. 2013 and

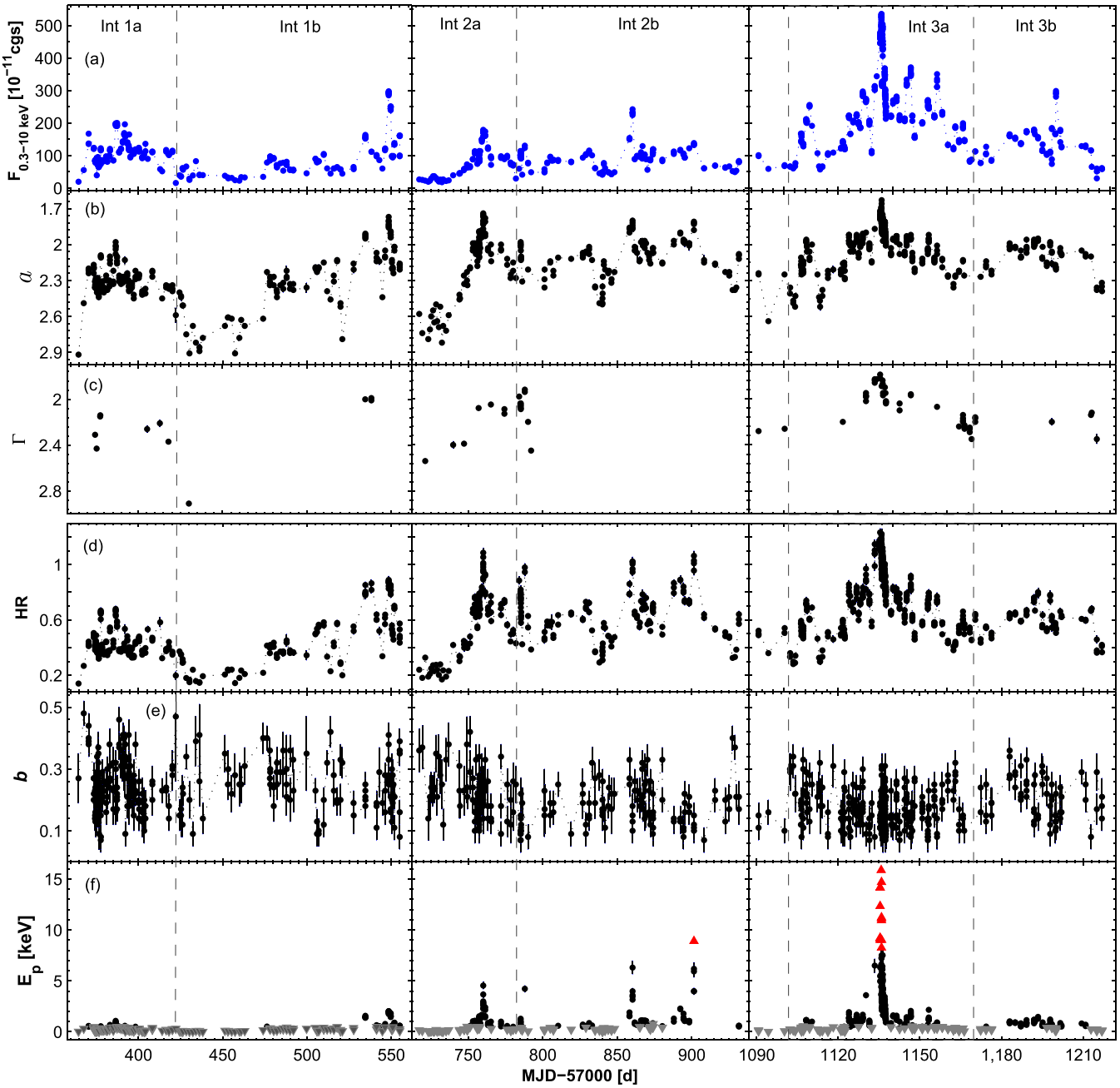

Figure 10. De-absorbed 0.3–10 keV flux and different spectral parameters plotted vs. time. The gray and red triangles in the bottom panel indicate the upper and lower limits to the intrinsic position of the synchrotron SED peak, respectively.

Table 10
The Results of the XRT Spectral Analysis with a Simple Power-law Model

ObsID (1)	Γ (2)	$10 \times K$ (3)	χ^2/dof (4)	$F_{0.3-2\ keV}$ (5)	$F_{2-10\ keV}$ (6)	$F_{0.3-10\ keV}$ (7)	HR (8)
35014245 Or5	2.31(0.02)	1.73(0.02)	0.95/186	57.68(0.66)	28.12(0.83)	85.90(1.18)	0.49(0.02)
35014246 Or4	2.43(0.02)	1.51(0.02)	0.88/182	52.60(0.60)	20.70(0.52)	73.28(0.67)	0.39(0.01)
34228001 Or1 S2(410 s)	2.15(0.02)	1.64(0.02)	1.09/229	51.88(0.71)	33.81(0.77)	85.70(0.98)	0.65(0.02)
34228001 Or2 S2(285 s)	2.14(0.02)	2.32(0.02)	1.08/233	73.45(0.84)	48.42(1.10)	121.90(1.40)	0.66(0.02)
34228023	2.26(0.03)	1.77(0.03)	0.91/139	58.34(1.06)	31.05(1.26)	89.33(1.43)	0.53(0.02)

Note. See the corresponding machine-readable table for the full version. Col. (1): ObsID of the particular observation, along with the duration of the separate segments (in seconds) used to extract a spectrum in parentheses. The acronyms "Or" and "S" stand for "orbit" and "segment," respectively. Col. (2): value of the 0.3–10 keV photon index. Cols. (3) and (4): norm and reduced χ^2, respectively. Cols. (5)–(7): de-absorbed 0.3–2, 2–10, and 0.3–10 keV in erg cm^{-2} s^{-1}. Col. (8): HR.

(This table is available in its entirety in machine-readable form.)

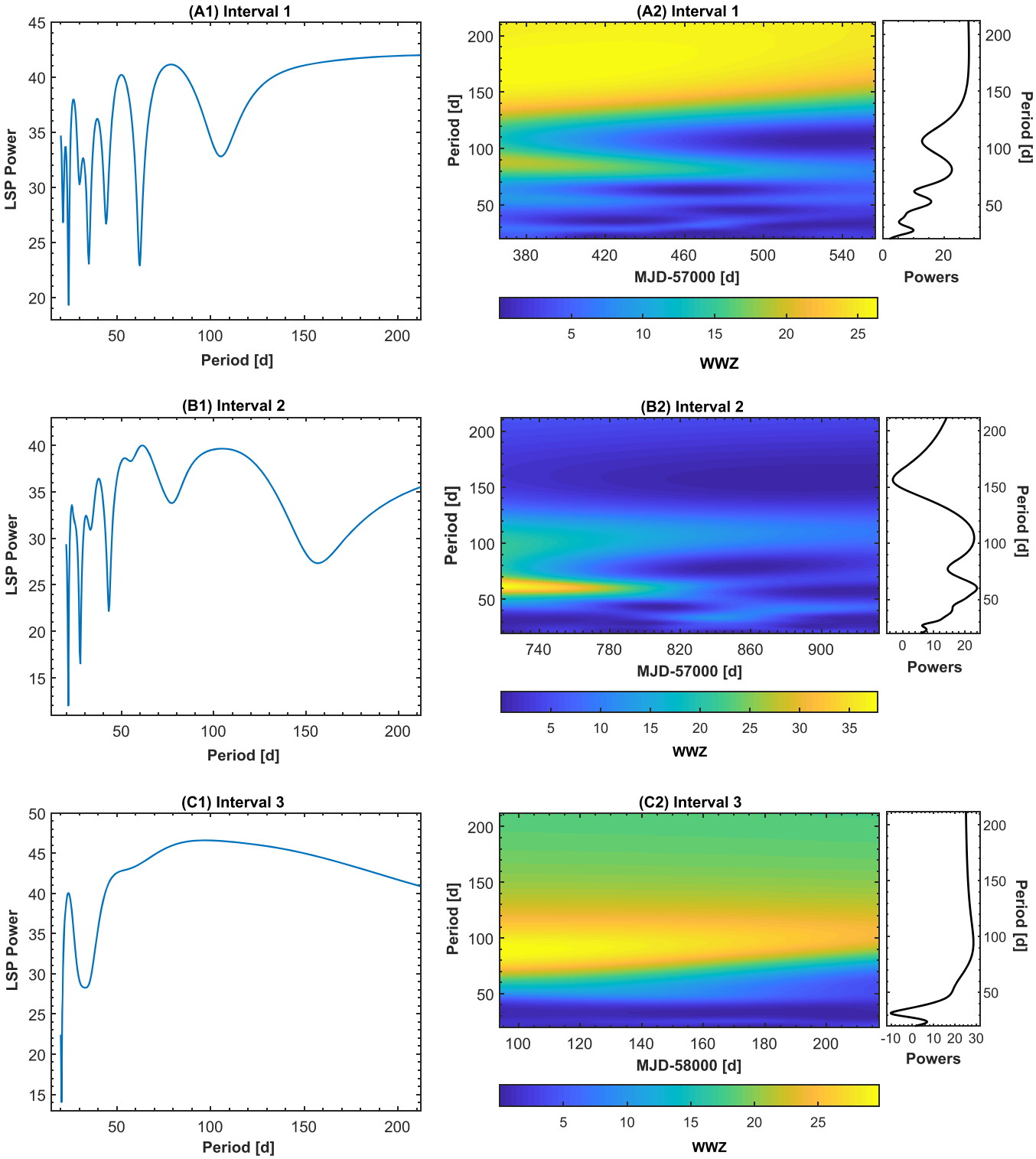

Figure 11. The LSP and WWZ plots from the XRT observations of Mrk 421 in different intervals.

references therein)

$$R_{\rm em} \leqslant \frac{c\tau_{\rm d}\Gamma_{\rm em}}{1+z}, \tag{7}$$

where $R_{\rm em}$ and $\Gamma_{\rm em}$ are the size and Lorentz factor of the emission zone, respectively. Adopting the typical value of the bulk Lorentz factor for the emission zone $\Gamma_{\rm em} = 10$ (Falomo et al. 2014), we obtain upper limits of 5.0×10^{15}–1.9×10^{16} cm for the emission zones with intraday flux doubling instances. More extreme behavior was exhibited by Mrk 421 during the densely sampled *Swift*-XRT campaign of 2009 May 22–27 (net exposure time of 23.5 ks, 59 orbits), $\tau_{\rm h} = 1.4$–1.5 hr and $\tau_{\rm d} = 6.5$–12.4 hr (Kapanadze et al. 2018b). A series of brightness halving and doubling events with $\tau_{\rm d,h} \sim 1.1$ hr was recorded on 2009 February 17, and a similar variability also occurred during 2017 February 2–3 (see Section 3.1 and Figure 1(i)). Note that the

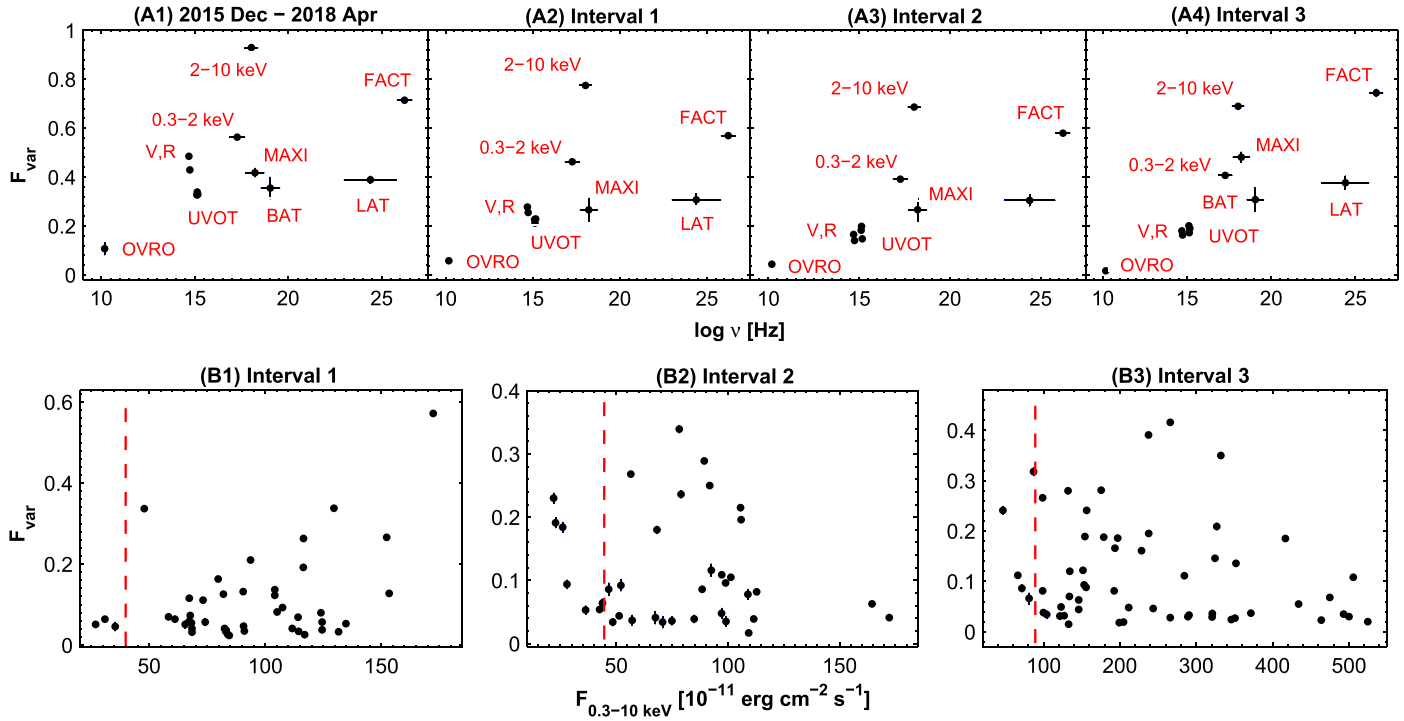

Figure 12. Panels (A1)–(A4): multi-instrument fractional amplitude $F_{\rm var}$ as a function of the energy in different periods. Panels (B1)–(B3): $F_{\rm var}$ of the 0.3–10 keV IDVs as a function of the flux in different periods. In each plane, a vertical red dashed line represents the threshold below which the low X-ray states were observed (see the text for the quantitative definition).

successive large brightness drop and rise events can be explained as a consequence of a shock passage through two inhomogeneous areas with strong magnetic fields, which are separated by a region with a significantly weaker field and lower particle density (yielding a generation of fewer X-ray photons). The most extreme behavior was observed during the giant X-ray outburst in 2013 April, with several events showing $\tau_{\rm d} = 1.2$–7.2 hr and $\tau_{\rm h} = 1.0$–3.5 hr (Kapanadze et al. 2016).

The distribution of the 0.3–10 keV fluxes extracted from those *Swift*-XRT pointings that showed IDVs in the period 2015 December–2018 April is not well fitted with the lognormal function, in contrast to the longer-term flares. This result hints at the absence of an AD variability imprint onto these events. Moreover, Figures 12(B1)–(B3) show a rare occurrence of these events in low X-ray states[19] when the IDVs caused by the instability in AD or the inner jet regions should be more easily detectable: the variable emission from these regions will not be "overwhelmed" by the huge flux produced near the shock front, propagating through the jet and causing longer-term flares (see Mangalam & Wiita 1993 and references therein). On the other hand, most of these events are detected from short XRT exposures, and the entire cycle (brightness increase and drop) is generally not recorded, in contrast to the longer-term flares. Therefore, it is not possible to draw a firm conclusion about the absence of lognormality. However, the 0.3–10 keV flux values from those IDVs whose complete variability cycles were observed do not exhibit a lognormal flux distribution. Therefore, these results favor the "shock-in-jet" scenario where IDVs are triggered by the interaction of a shock front with small-size jet inhomogeneities (Sokolov et al. 2004; Marscher 2014; Mizuno et al. 2014).

The duty cycle of the 0.3–10 keV IDVs (i.e., the fraction of total observation time during which the object displayed IDVs; see Romero et al. 1999 and references therein) amounted to 58.4%, which is higher than that shown by the source in 2009–2012 and 2013 November–2015 June (43%–46%; Kapanadze et al. 2017a, 2018b) but significantly lower than compared to the periods 2005–2008 and 2013 January–May (about 84%; Kapanadze et al. 2016, 2018a). Note that this result can be partially related to significantly more densely sampled campaigns in some parts of the latter periods. For example, Mrk 421 was observed very densely during 2006 June 15–25 with a total exposure of 119 ks distributed over 124 *Swift*-XRT orbits.

On the other hand, the source exhibited unequal 0.3–10 keV activity on intraday timescales in different epochs. Note that the XRT pointings without IDVs were mainly performed during the lower X-ray states. However, we also discerned some flares with a clear lack of intraday activity. For example, such flaring activity was observed during MJD 57,521–57,548 with $\rm CR_{max} = 95.73 \pm 0.32$ counts $\rm s^{-1}$, which is a factor of 2.5 higher than the mean rate during the whole period 2015 December–2018 April. This event was preceded by the long time interval (MJD 57,400–57,520) when the source showed the lowest mean rate (23.24 ± 0.01 counts $\rm s^{-1}$) and duty cycle of IDVs (36%) for the entire 2015–2018 period. A similar situation was observed in 2010 June–July when the source demonstrated low 0.3–10 keV states with CR ~ 10 counts $\rm s^{-1}$ and insignificant variability over 1.5 months, possibly related to the absence of strong shock waves, which could cause a long-term flare in different spectral bands (Kapanadze et al. 2018b). Moreover, the source also showed significantly slower and weaker IDVs during those densely sampled XRT observations presented in Figure 4. These results

[19] The de-absorbed 0.3–10 keV flux values, corresponding to the low X-ray states of the source, were below the thresholds of about 4.0×10^{-10}, 4.5×10^{-10}, and 9.0×10^{-10} cgs in intervals 1, 2, and 3, respectively.

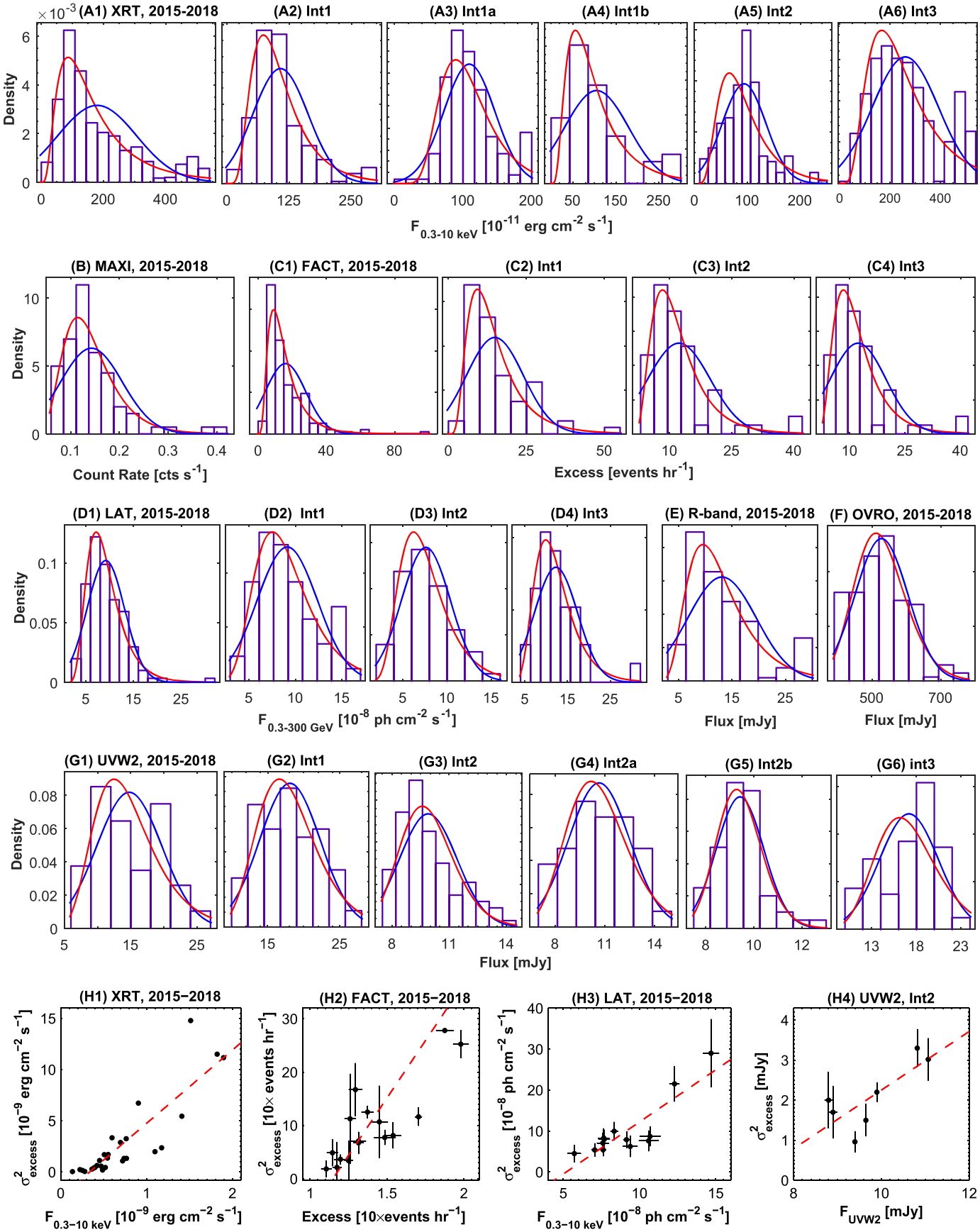

Figure 13. Histograms of the MWL fluxes. In each plot, red and blue lines correspond to the lognormal and Gaussian fits, respectively. For space reasons, the period 2015 December–2018 April is denoted as "2015–2018" in the plot titles. The bottom row shows scatter plots with $\sigma^2_{\rm excess}$ and the average flux for the MWL data. A linear fit is shown by the red dashed line.

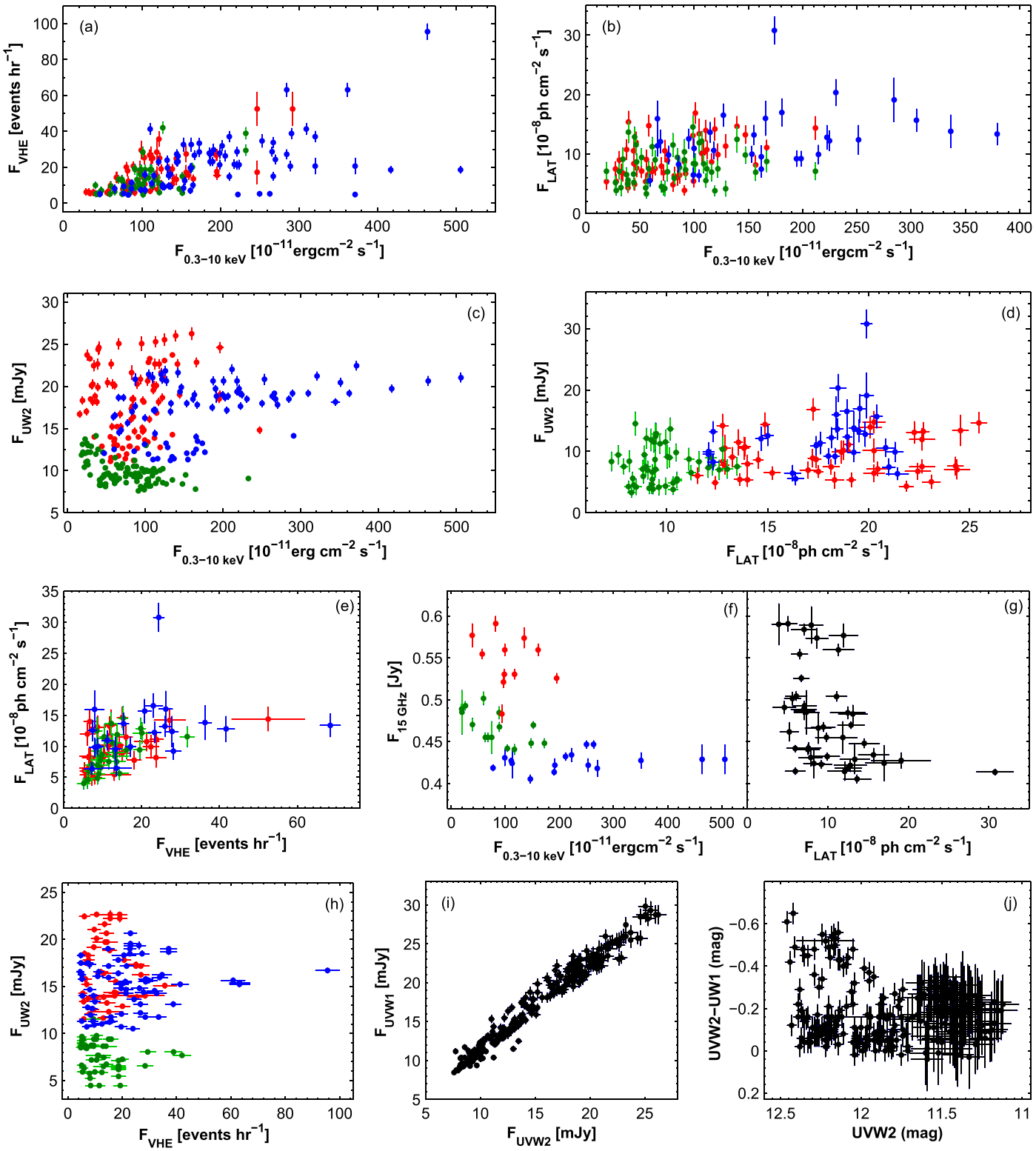

Figure 14. Correlations between the MWL fluxes. The colored points in Figures 14(a)–(h) correspond to the different periods as follows: red—interval 1, green—interval 2, blue—interval 3.

lead to the conclusion that the source underwent weaker variability on intraday timescales during the low X-ray states and some longer-term flares.

The last column of Table 4 provides a list of the variable spectral factors presumably making the dominant contribution to the particular 0.3–10 keV IDV. The most common factor in the observed fast variability was a change of the photon index (i.e., in the slope of the particle energy distribution (PED)). Nevertheless, some events were related to the transition from a log-parabolic PED to a power-law one and/or vice versa. The most extreme log-parabolic/power-law/log-parabolic transitions occurred within the 1 ks exposures during ObsID 31202174

(MJD 58,135.39), the fourth orbit of ObsID 31202175 (MJD 58,136.33), and the first orbit of ObsID 31202178 (MJD 58,137.11) in the epoch of the strongest X-ray flaring activity of the source during 2015–2018. Such extreme events can be related to the very fast variability of the magnetic field properties within the jet regions that are smaller than $R = 10^{14}$ cm (for $\delta = 10$): a transition from a magnetic field characterized by decreasing confinement efficiency with a rising electron's gyroradius or strong turbulence (both yielding a log-parabolic PED) into a volume without these properties, and vice versa (see below). A number of the IDVs were also related to the variability of the curvature parameter and the position and height of the synchrotron SED peak. The changes of the latter two quantities imply an intraday and even a subhour variability of the physical parameters (magnetic field, Doppler factor, γ^2_{3p}: the peak of the function $n(\gamma)\gamma^3$) included in the relations as follows (Rybicki & Lightman 1979 and references therein):

$$E_p \propto \gamma^2_{3p} B\delta, \quad S_p \propto N\gamma^2_p B^2\delta^4. \tag{8}$$

4.2. MWL Correlations

During the time interval presented in this work, the TeV-band variability showed the strongest correlation with the X-ray one: strong VHE flares or enhanced activity mostly coincided with strong X-ray flares (see Section 3.2). Consequently, Figure 14(a) shows a positive $F_{0.3\text{–}10\text{keV}}$–$F_{\text{VHE}}$ correlation in each interval, although it was relatively weak in interval 3 compared to that in interval 1 (the difference between the values of the coefficient ρ was larger than the corresponding error ranges; see Table 11). In fact, some data points from interval 3 are the largest exceptions from the general trend. Such a situation was particularly evident during MJD 58,145–58,153 (interval 3a): the VHE flux showed a decline by a factor of ∼4 and subsequent low states during the fast X-ray flare with one of the highest states during the 2015–2018 period (see Figure 6(a)). Two data points in the lower right corner of the $F_{0.3\text{–}10\text{keV}}$–$F_{\text{VHE}}$ plane belong to the X-ray flare around MJD 58,136, when the 0.3–10 keV flux reached its highest values, while the TeV-band state was the highest on the previous day. This situation is hard to reconcile with one-zone SSC scenarios (Blazejowski et al. 2005). However, Figure 7(a) demonstrates that no strictly simultaneous XRT observation was performed during those 20 minute FACT pointings detecting the source in the highest VHE states. Therefore, we cannot draw any firm conclusions for this case.

The source was not detectable with 3σ or showed low VHE states when it had undergone short-term X-ray flares during MJD(57)413–422 (Figure 6(c)), MJD(57)425–438 and MJD (57)473–491 (Figure 6(d)), and MJD(57)723–730 and MJD (57)801–838(Figure 6(e)). Similar instances were reported from the FACT observations of Mrk 421 performed in previous years (Kapanadze et al. 2016, 2017a). Moreover, the MWL campaign in 2002 December–2003 January revealed a strong X-ray flare of a factor of 7 within 3 days not accompanied by a comparable TeV counterpart (Rebillot et al. 2006). The TeV flux reached its peak days before the X-ray flux during the giant flare in 2004 that was impossible to explain via the standard one-zone SSC model, and Blazejowski et al. (2005) suggested this as an instance of the "orphan" TeV flare. Acciari et al. (2011) also found high X-ray states not accompanied by TeV flaring, and vice versa, in 2006–2008. We conclude that the broadband SED cannot always be modeled using one-zone SSC scenarios, although they were acceptable for Mrk 421 during the majority of the X-ray flares (corroborated by the appearance of a two-hump structure in the F_{var}–logν plane, with the peaks at X-ray and TeV frequencies, respectively).

The 0.3–10 keV variability showed a weak positive correlation with that observed in the MeV–GeV energy range (see Figure 14(b) and Table 11). The source did not undergo comparable LAT-band activity or exhibited lower states during the most extreme X-ray behavior (MJD 58,115–58,160;

Table 11
Correlations between the MWL Fluxes (Denoted by "F_i" for the Particular i-band in Column 1) during Different Periods

Quantities	ρ	p
	2015 Dec–2018 Apr	
$F_{0.3\text{–}2\ \text{keV}}$ and $F_{2\text{–}10\ \text{keV}}$	0.93(0.02)	$<10^{-15}$
$F_{0.3\text{–}10\ \text{keV}}$ and F_{FACT}	0.61(0.08)	5.44×10^{-10}
$F_{0.3\text{–}10\ \text{keV}}$ and F_{UVW2}	0.30(0.11)	4.07×10^{-5}
$F_{0.3\text{–}10\ \text{keV}}$ and F_{UVW1}	0.25(0.11)	8.34×10^{-4}
$F_{0.3\text{–}10\ \text{keV}}$ and F_{LAT}	0.49(0.10)	1.03×10^{-8}
$F_{0.3\text{–}10\ \text{keV}}$ and F_{15GHz}	−0.53(0.09)	8.89×10^{-9}
F_{UVM2} and F_{UVW2}	0.94(0.02)	$<10^{-15}$
F_{UVW1} and F_{UVW2}	0.96(0.01)	$<10^{-15}$
F_{UVW2} and F_{LAT}	0.32(0.11)	7.58×10^{-5}
F_{FACT} and F_{LAT}	0.55(0.09)	1.24×10^{-9}
F_{LAT} and F_{15GHz}	−0.49(0.14)	3.55×10^{-4}
$F_{0.3\text{–}2\ GeV}$ and $F_{2\text{–}300\ GeV}$	0.75(0.06)	5.02×10^{-13}
	Int 1	
$F_{0.3\text{–}2\ \text{keV}}$ and $F_{2\text{–}10\ \text{keV}}$	0.88(0.03)	$<10^{-15}$
$F_{0.3\text{–}10\ \text{keV}}$ and F_{FACT}	0.62(0.07)	1.28×10^{-11}
$F_{0.3\text{–}10\ \text{keV}}$ and F_{LAT}	0.44(0.10)	6.10×10^{-8}
F_{FACT} and F_{LAT}	0.45(0.10)	3.71×10^{-8}
	Int 1a	
$F_{0.3\text{–}10\ \text{keV}}$ and F_{UVW2}	0.56(0.11)	5.01×10^{-5}
$F_{0.3\text{–}10\ \text{keV}}$ and F_{UVW1}	0.48(0.12)	7.79×10^{-5}
	Int 1b	
$F_{0.3\text{–}10\ \text{keV}}$ and F_{UVW2}	−0.46(0.11)	6.77×10^{-5}
$F_{0.3\text{–}10\ \text{keV}}$ and F_{UVW1}	−0.43(0.11)	3.40×10^{-5}
	Int 2	
$F_{0.3\text{–}2\ \text{keV}}$ and $F_{2\text{–}10\ \text{keV}}$	0.93(0.02)	$<10^{-15}$
$F_{0.3\text{–}10\ \text{keV}}$ and F_{FACT}	0.51(0.09)	7.76×10^{-9}
$F_{0.3\text{–}10\ \text{keV}}$ and F_{UVW2}	−0.45(0.09)	1.08×10^{-6}
$F_{0.3\text{–}10\ \text{keV}}$ and F_{UVW1}	−0.47(0.09)	2.03×10^{-7}
$F_{0.3\text{–}10\ \text{keV}}$ and F_{LAT}	0.34(0.12)	3.17×10^{-4}
$F_{0.3\text{–}10\ \text{keV}}$ and F_{15GHz}	−0.71(0.09)	3.33×10^{-9}
F_{FACT} and F_{LAT}	0.64(0.08)	6.10×10^{-11}
	Int 2a	
$F_{0.3\text{–}10\ \text{keV}}$ and F_{UVW2}	−0.75(0.09)	1.92×10^{-8}
$F_{0.3\text{–}10\ \text{keV}}$ and F_{UVW1}	−0.74(0.09)	4.56×10^{-8}
	Int 3	
$F_{0.3\text{–}2\ \text{keV}}$ and $F_{2\text{–}10\ \text{keV}}$	0.93(0.03)	$<10^{-15}$
$F_{0.3\text{–}10\ \text{keV}}$ and F_{FACT}	0.45(0.11)	9.01×10^{-8}
$F_{0.3\text{–}10\ \text{keV}}$ and F_{UVW2}	0.39(0.10)	4.07×10^{-5}
$F_{0.3\text{–}10\ \text{keV}}$ and F_{UVW1}	0.38(0.10)	9.95×10^{-5}
$F_{0.3\text{–}10\ \text{keV}}$ and F_{LAT}	0.39(0.11)	5.26×10^{-4}

Note. In the second and third columns, ρ and p stand for the Spearman coefficient and corresponding p-chance, respectively.

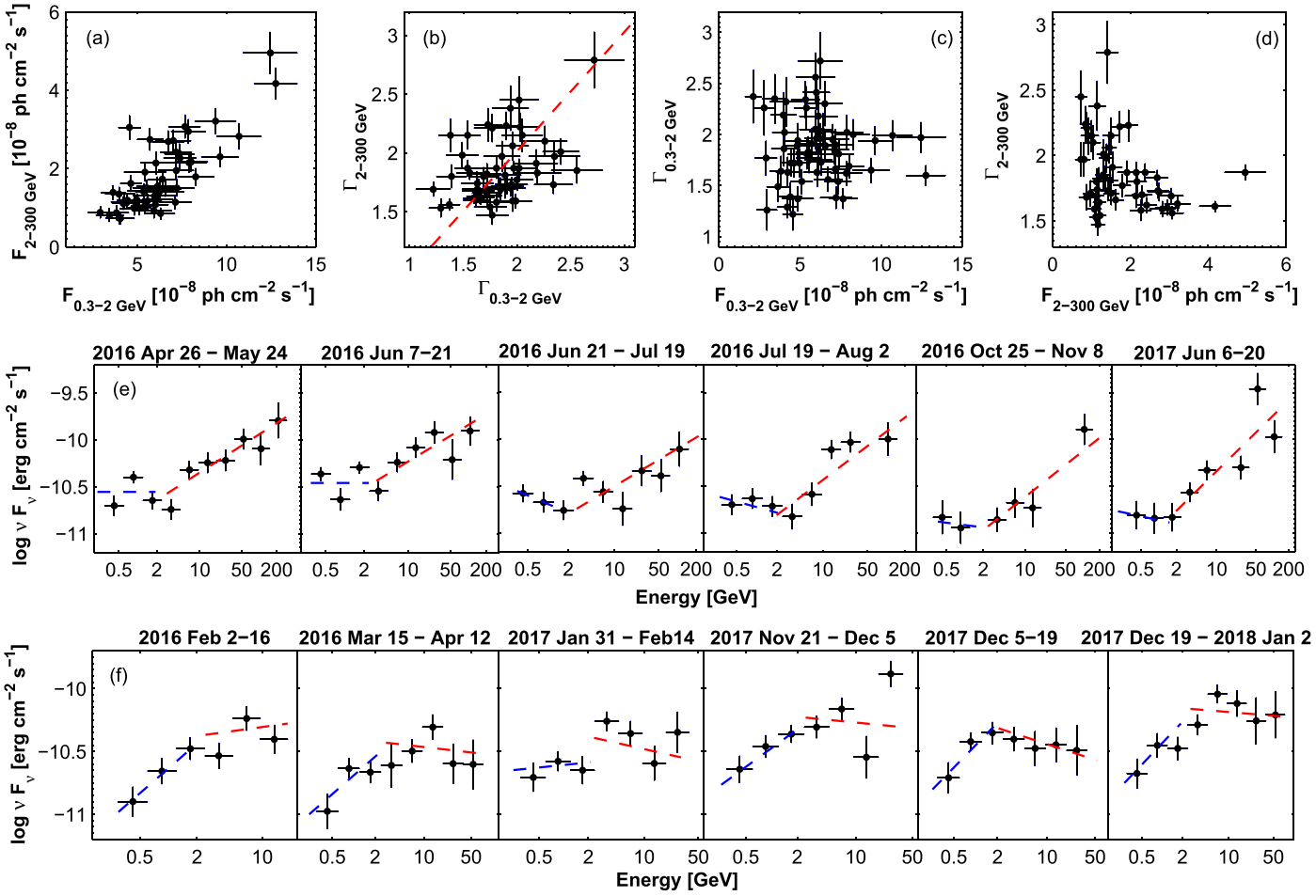

Figure 15. Results from 2-weekly binned LAT data for the period 2015 December–2018 April. The scatter plots are as follows: 0.3–2 and 2–300 GeV photon fluxes (panel (a)); 0.3–2 and 2–300 GeV photon indices, with the red dashed line corresponding to $\Gamma_{0.3-2\mathrm{GeV}} = \Gamma_{2-300\mathrm{GeV}}$ (panel (b)); 0.3–2 GeV photon flux and index (panel (c)); and 2–300 GeV photon flux and index (panel (d)). Panels (e) and (f) give the 0.3–300 GeV SEDs from the time intervals showing a hardening and softening in the 2–300 GeV energy range, respectively. The blue and red dashed lines represent linear fits to the 0.3–2 and 2–300 GeV SEDs, respectively.

Figure 6(a)). Moreover, no credible detections or low fluxes were recorded in the time intervals MJD(58)190–215 and (57) 364–381 (Figures 6(b)–(c)) and MJD(57)731–746 (Figure 6(e)). An even weaker $F_{0.3-10\mathrm{keV}}$–$F_{0.3-300\mathrm{GeV}}$ correlation was observed during 2009–2012 and 2013 January–June, while no significant correlation was found for the period 2013 November–2015 June (Kapanadze et al. 2016, 2017a, 2018b).

We extracted the 0.3–2 and 2–300 GeV photon fluxes from the LAT observations to check their cross-correlation and search for possible contributions from different electron populations to the LAT-band emission. We used two weekly binned observations to ensure $N_{\mathrm{pred}} \geqslant 10$ (Table 12). Figure 15(a) exhibits a strong $F_{0.3-2\mathrm{GeV}}$–$F_{2-300\mathrm{GeV}}$ correlation, demonstrating a predominantly common origin for the soft and hard LAT-band photons. This result is in contrast to that obtained for 1ES 1959+650 during the period 2016 August–2017 November, with a weak correlation between the softer and harder LAT-band fluxes that hints at uncorrelated behavior and a possible contribution from different particle populations (Kapanadze et al. 2018e).

Note that the LAT-band flux was also correlated weakly with the UVOT- and FACT-band fluxes, respectively (see Figures 14(d) –(e)). This result can be explained as an IC upscatter of the UV photons to the MeV–GeV energies in the Thomson regime (a similar relation between the X-ray and VHE photons). Another source of the LAT-band emission can be an upscatter of X-ray photons in the Klein–Nishina (K–N) regime. An upscatter of the BAT-band photons in the same regime could be the case during those time intervals when the source showed low VHE states with the absent $F_{0.3-10\mathrm{keV}}$–F_{VHE} correlation or was not detectable in the TeV energy range (owing to strong suppression of the γ-ray emission in this regime; see Tramacere et al. 2009).

Both LAT- and XRT-band fluxes showed an anticorrelation with the 15 GHz emission that was particularly strong in interval 2 in the case of the X-ray emission (see Figures 14(f)–(g) and Table 11). A similar situation is evident from the scatter plot $F_{0.3-10\mathrm{keV}}$–F_{UVW2} constructed for intervals 2 and 1b (Figure 14(c) and the aforementioned table). Such a feature was also reported by Alecsic et al. (2015b) and explained through a hardening of the electron energy distribution that can shift the entire synchrotron bump to higher energies. Consequently, the emission of the synchrotron SED in the radio–UV energy range is expected to decrease with rising X-ray brightness. Note that such MWL behavior is expected for the stochastic acceleration of electrons within the specific initial conditions (see Section 4.3).

No $F_{0.3-10\mathrm{keV}}$–F_{UVW2} correlation at the 99% confidence level was detected in interval 1, and a very weak positive correlation

Table 12
The Results from 2-weekly Binned LAT Data in the 0.3–2 and 2–300 GeV Bands

	0.3–2 GeV				2–300 GeV				
Dates	TS	$N_{\rm pred}$	Flux	Γ	TS	$N_{\rm pred}$	Flux	Γ	Remark
(1)	(2)	(3)	(4)	(5)	(6)	(7)	(8)	(9)	(10)
2015 Dec 8−Aug 22	55.0	143.5	6.05(0.85)	1.63(0.14)	175.8	24.6	2.14(0.29)	1.69(0.09)	3
2015 Dec 22−2016 Jan 5	113.1	380.1	7.67(0.88)	1.37(0.10)	639.9	55.9	3.07(0.30)	1.56(0.05)	2
2016 Jan 5−Jan 19	80.5	274.8	9.39(1.15)	1.65(0.12)	481.4	40.4	3.21(0.33)	1.63(0.06)	3
2016 Jan 19−Feb 2	80.5	256.1	7.86(0.96)	1.62(0.12)	400.8	37.6	2.95(0.31)	1.60(0.06)	3
2016 Feb 2−Feb 16	62.7	183.7	4.56(0.62)	1.22(0.16)	482.6	47.0	3.05(0.31)	1.69(0.06)	2
2016 Feb 16−Mar 1	103.0	280.5	8.28(1.02)	2.00(0.15)	257.0	28.6	1.79(0.22)	1.77(0.09)	3
2016 Mar 1−Mar 15	51.4	143.9	4.64(0.60)	1.72(0.14)	247.3	22.4	1.62(0.21)	1.66(0.08)	3
2016 Mar 15−Mar 29	43.2	108.5	3.65(0.69)	1.49(0.15)	178.0	20.1	1.39(0.18)	1.98(0.11)	2
2016 Mar 29−Apr 12	57.7	136.5	4.41(0.71)	1.39(0.14)	153.8	18.0	1.13(0.16)	1.80(0.10)	2
2016 Apr 12−Apr 26	61.9	144.0	5.40(0.76)	2.26(0.21)	95.4	16.2	1.04(0.20)	2.10(0.13)	2
2016 Apr 26−May 10	58.6	166.9	6.02(0.72)	1.96(0.12)	126.2	13.4	1.08(0.18)	1.59(0.09)	1
2016 May 10−May 24	60.5	179.6	7.39(0.91)	1.81(0.15)	274.3	23.3	2.27(0.27)	1.58(0.08)	3
2016 May 24−Jun 7	80.4	208	6.41(0.82)	2.03(0.18)	216.3	28.1	1.73(0.23)	2.22(0.12)	3
2016 Jun 7−Jun 21	110.6	353.7	9.64(1.04)	1.94(0.14)	334.2	33.4	2.30(0.26)	1.70(0.07)	1
2016 Jun 21−Jul 5	44.3	101.1	6.14(1.18)	2.18(0.20)	111.0	14.3	1.54(0.25)	1.91(0.12)	1
2016 Jul 5−Jul 19	46.7	99.8	5.97(1.20)	2.56(0.24)	144.9	13.5	1.30(0.20)	1.85(0.11)	1
2016 Jul 19−Aug 2	64.8	156.6	5.57(0.80)	1.77(0.15)	177.9	17.2	1.17(0.18)	1.47(0.08)	1
2016 Aug 2−Aug 16	37.7	106.2	6.54(1.08)	2.30(0.22)	66.4	7.7	1.54*	⋯	
2016 Aug 16−Aug 30	39.7	109.5	3.84(0.69)	1.64(0.15)	86.7	11.2	0.87(0.19)	1.68(0.10)	3
2016 Aug 30−Sep 13	36.7	70.2	2.92(0.68)	1.77(0.17)	118.2	13.9	0.88(0.15)	2.21(0.12)	2
2016 Sep 13−Sep 27	25.9	31.5	2.12(0.50)	2.37(0.26)	38.4	6.7	1.32*	⋯	
2016 Sep 27−Oct 11	28.0	56.7	4.15(1.00)	2.32(0.24)	6.1	3.2	1.56*	⋯	
2016 Oct 11−Oct 25	22.9	75.7	2.98(0.63)	1.26(0.20)	65.5	8.3	1.61*	⋯	
2016 Oct 25−Nov 8	32.1	55.3	3.45(0.77)	2.35(0.24)	81.6	9.9	0.81(0.17)	1.97(0.13)	1
2016 Nov 8−Nov 22	67.0	168.4	5.52(0.78)	1.83(0.15)	223.4	23.2	1.51(0.20)	1.71(0.09)	3
2016 Nov 22−Dec 6	55.0	201.8	5.12(0.67)	1.54(0.12)	103.4	13.4	1.00(0.19)	2.15(0.12)	2
2016 Dec 6−Dec 20	35.1	69.5	6.25(1.37)	2.72(0.28)	87.6	10.5	1.41(0.28)	2.79(0.24)	3
2016 Dec 20−2017 Jan 3	75.1	187.2	6.57(0.87)	1.89(0.15)	175.1	21.6	1.48(0.20)	1.81(0.10)	3
2017 Jan 3−Jan 17	94.8	246.7	7.90(1.01)	2.02(0.17)	317.0	33.0	2.15(0.24)	1.87(0.08)	3
2017 Jan 17−Jan 31	61.7	186.3	6.14(0.86)	1.75(0.15)	155.7	15.4	1.22(0.16)	1.54(0.08)	3
2017 Jan 31−Feb 14	89.7	205.9	7.19(0.99)	1.90(0.15)	262.1	29.9	1.95(0.23)	2.23(0.12)	2
2017 Feb 14−Feb 28	69.3	217.0	5.72(0.74)	1.91(0.15)	393.7	43.7	2.74(0.28)	1.72(0.07)	3
2017 Feb 28−Mar 14	46.2	111.8	4.02(0.78)	1.86(0.17)	72.3	10.7	0.73(0.15)	1.97(0.13)	3
2017 Mar 14−Mar 28	63.6	195.6	6.31(0.80)	1.73(0.13)	90.2	10.9	0.85(0.15)	2.24(0.14)	
2017 Mar 28 Apr 11	73.2	210.9	4.45(0.58)	1.72(0.13)	212.2	24.4	1.19(0.16)	1.82(0.09)	2
2017 Apr 11−Apr 25	100.5	301.6	8.03(0.92)	1.69(0.12)	331.6	34.1	2.17(0.25)	1.80(0.08)	3
2017 Apr 25−May 9	58.4	164.5	4.98(0.69)	1.72(0.14)	176.1	17.6	1.20(0.16)	1.64(0.09)	2
2017 May 9−Sep 23	46.1	112.5	4.25(0.72)	1.63(0.15)	123.7	15.5	1.15(0.18)	1.74(0.10)	3
2017 May 23−Jun 6	48.5	111.2	5.94(0.98)	2.05(0.19)	70.0	9.8	0.93(0.20)	2.15(0.14)	3
2017 Jun 6−Jun 20	50.5	90.2	3.98(0.78)	2.19(0.22)	216.3	22.3	1.35(0.18)	1.83(0.09)	2
2017 Jun 20−Jul 4	26.7	39.5	2.80(0.66)	2.26(0.27)	35.9	5.2	1.42*	⋯	
2017 Jul 4−Jul 18	31.1	98.6	4.87(0.97)	1.37(0.12)	71.3	6.4	1.82*	⋯	
2017 Jul 18−Aug 1	75.8	171.7	6.24(0.83)	1.96(0.15)	194.0	23.2	1.46(0.19)	2.06(0.12)	3
2017 Aug 1−Aug 15	49.6	107.7	4.06(0.78)	2.02(0.18)	76.6	11.4	0.73(0.15)	2.45(0.20)	2
2017 Aug 15−Aug 29	49.6	121.7	4.84(0.80)	1.89(0.17)	112	12.7	0.98(0.18)	1.71(0.10)	3
2017 Aug 29−Sep 12	52.1	141.5	4.22(0.62)	1.29(0.11)	149.4	16.6	1.11(0.16)	1.53(0.08)	2
2017 Sep 12−Sep 26	83.8	195.2	7.14(0.90)	1.85(0.14)	126.4	17.0	1.14(0.17)	1.69(0.10)	3
2017 Sep 26−Oct 10	49.0	114.7	5.35(0.88)	2.34(0.18)	223.0	23.1	1.42(0.18)	1.73(0.08)	1
2017 Oct 10−Oct 24	58.0	134.7	4.87(0.80)	1.94(0.17)	98.5	13.8	1.15(0.22)	2.38(0.19)	2
2017 Oct 24−Nov 7	67.4	173.9	5.43(1.18)	1.81(0.15)	280.7	29.9	1.91(0.24)	1.87(0.09)	3
2017 Nov 7−Nov 21	84.1	147.2	6.02(0.84)	2.41(0.17)	216.2	24.2	1.31(0.17)	2.01(0.11)	1
2017 Nov 21−Dec 5	96.1	284.1	7.36(0.84)	1.54(0.12)	353.6	38.2	2.38(0.26)	1.87(0.07)	2
2017 Dec 5−Dec 19	63.3	248.0	7.22(0.98)	1.38(0.11)	152.5	15.8	1.50(0.21)	2.15(0.14)	2
2017 Dec 19−2018 Jan 2	73.8	206.6	6.74(0.87)	1.56(0.12)	387.7	36.2	2.69(0.28)	1.83(0.06)	2
2018 Jan 2−Jan 16	98.8	264.9	7.18(0.88)	1.66(0.13)	360.5	41.6	2.42(0.26)	1.62(0.06)	3
2018 Jan 16−Jan 30	86.6	279.7	10.71(1.24)	1.99(0.15)	321.5	29.0	2.82(0.33)	1.59(0.06)	1
2018 Jan 30−Jan 13	73.8	255.8	12.46(1.52)	1.97(0.15)	386.0	37.3	4.95(0.53)	1.87(0.06)	3
2018 Feb 13−Feb 27	161.5	587.7	12.77(1.21)	1.60(0.10)	748.9	65.5	4.17(0.40)	1.61(0.04)	3
2018 Feb 27−Mar 13	86.4	208.6	7.02(1.01)	1.95(0.15)	434.1	42.5	2.71(0.28)	1.73(0.06)	1

Note. Cols. (2) and (6): TS corresponding to Mrk 421 in each band. Cols. (3) and (7): number of model-predicted photons. Cols. (4) and (8): photon fluxes in units of 10^{-8} ph cm^{-2} s^{-1}. Cols. (5) and (9): 0.3–2 and 2–300 GeV photon indices, respectively. Col. (10) provides a remark related to the interplay between the 0.3–2 and 2–300 GeV spectral hardnesses: 1—increasing hardness with energy; 2—harder spectra in the 0.3–2 GeV energy range; 3—no significant difference between the higher- and lower-energy photon indices. In col. (8), an asterisk stands for the upper limit to the 2–300 GeV flux.

occurred in interval 3. An anticorrelation was also observed during 2009–2012, and uncorrelated variabilities occurred in 2005–2008 and 2014 February–2015 June (Kapanadze et al. 2017a, 2018b). A stronger positive correlation was observed during 2013 January–June and 2013 November–2014 January (Kapanadze et al. 2016, 2017a). We have not found a correlation between the UV and VHE fluxes, hinting at an insignificant role for the upscatter of the UV photons to VHE frequencies in the Thomson regime (Figure 14(h)). Finally, the *UVW1–UVW2* fluxes showed very strong cross-correlations, as in previous periods, reflected in the absence of the UV color variability and demonstrating the generation of these photons by the same electron population via the synchrotron mechanism in each period (Figures 14(i)–(j)).

4.3. Spectral Properties and Particle Acceleration Processes

4.3.1. First-order Fermi Acceleration

A positive *a–b* correlation (see Figure 9(a)), detected in intervals 1–3, shows the importance of the first-order Fermi acceleration, since this correlation was predicted for those jet regions where particles are confined by a magnetic field at the shock front, whose confinement efficiency is declining with increasing gyration radius (i.e., the particle's energy; the so-called energy-dependent acceleration probability process (EDAP); Massaro et al. 2004). Consequently, the probability $_{pi}$ that a particle undergoes an acceleration step i with the corresponding energy γ_i^q and energy gain ε is given by $p_i = g/\gamma_i^q$, where g and q are positive constants. Consequently, the probability of the particle's acceleration is lower when its energy increases, and the differential energy spectrum is given by $N(\gamma) \sim \gamma/\gamma_0^{-s-r\log\gamma/\gamma_0}$, with a linear relationship between the spectral index and curvature terms (s and r, respectively) $s = -r(2/q)\log g/\gamma_0 - (q-2)/2$. The synchrotron emission produced by this distribution is given by

$$P_S(\nu) \propto (\nu/\nu_0)^{-(a+b\log(\nu/\nu_0))}, \quad (9)$$

with $a = (s-1)/2$ and $b = r/4$ (Massaro et al. 2004). However, the detected *a–b* correlation was weak in each interval. This result can be explained due to the subsamples having different slopes in the *a–b* plane, leading to a large scatter of the data points during the entire period 2015 December–2018 April. Note that some subsamples even showed a negative *a–b* trend (e.g., those corresponding to the short-term flares recorded during MJD 57,364–57,375, 57,395–57,408, and 57,527–57,544 in interval 1), which is expected when $g > \gamma_0$, i.e., there were electron populations with a very low initial energy γ_0 in the emission zone. Moreover, the coexistence of stochastic (second-order Fermi) acceleration could also weaken the aforementioned correlation, since the latter is not expected within the stochastic mechanism. The Monte Carlo simulations of Katarzynski et al. (2006) revealed that electrons can be accelerated at the shock front via EDAP and continue gaining energy via the stochastic mechanism into the shock downstream region (after escaping the shock front). After some time, a particle will be able to reenter the shock acceleration region and repeat the acceleration cycle. Consequently, such combined acceleration will not result in the strong *a–b* correlation.

A stronger positive *a–b* correlation was found for our target during the XRT observations in 2005–2008 and 2015 February ($\rho = 0.41$–0.57; Kapanadze et al. 2017a, 2018a). An even stronger correlation was reported by Massaro et al. (2004) from the *BeppoSAX* observations in 1997–2000. On the other hand, this correlation was weaker during 2009–2012 ($\rho = 0.21 \pm 0.07$) and absent in 2013 January–2014 June (Kapanadze et al. 2016, 2017a).

4.3.2. Stochastic Acceleration and Turbulence

As in previous years, the source mostly showed low curvatures ($b \sim 0.3$ or smaller for a vast majority of the log-parabolic spectra; see Section 3.3.1), i.e., a wider synchrotron SED, expected in the case of efficient stochastic acceleration (Massaro et al. 2011b). This result is related to the inverse proportionality of the PED curvature r to the diffusion coefficient D in the Fokker–Planck kinetic equation: $r \propto D^{-1}$. On the other hand, $r \propto \varepsilon/(n_s\sigma_\varepsilon^2)$ (Massaro et al. 2004), where n_s is the number of acceleration steps, and σ_ε^2 is the variance of the energy gain ε. Consequently, the detection of low spectral curvatures implies higher values of n_s and the diffusion coefficient, which needs strongly developed turbulence in a smaller acceleration region.

In fact, the relativistic magnetohydrodynamic simulations of Mizuno et al. (2014) showed that shock propagation can strongly amplify the turbulence in the shocked jet material due to its interaction with higher-density inhomogeneities existing in the preshock medium; the more frequent detection of the 0.3–10 keV IDVs in flaring X-ray states (compared to quiescence periods; see Section 4.1.3) demonstrates the viability of this scenario for Mrk 421 during the time interval presented in this work. Moreover, our detection of the anticorrelation $F_{0.3-10\mathrm{keV}}$–b (see Figure 9(c)), i.e., a dominance of lower curvatures in higher X-ray states, favors the shock-in-jet scenario and strongly developed turbulence during those states.

The simulations of Mizuno et al. (2014) also demonstrated that the higher-energy photons (including those having 0.3–10 keV energies) are expected to originate in the smallest jet regions, which contain the strongest magnetic field and yield the most rapid time variability. In fact, the fastest IDVs, occurring within a few hundred s, were observed mostly in the highest X-ray states in interval 3a, and such instances can be related to the interaction of the relativistic shock front with the smallest-scale turbulent regions, embodying stronger magnetic fields (according to the light-travel argument). Note also that this subinterval was remarkable for the lowest mean curvature observed in the whole 2015–2018 time interval, implying the existence of the most efficient stochastic acceleration in that subinterval.

Along with the flux, the 0.3–10 keV spectral parameters varied on intraday timescales. Sometimes, these changes were extremely fast, within 1 ks observational runs: curvatures rising by 0.19–0.22, hardenings by $\Delta a = 0.08$–0.23, shifts of the synchrotron SED peak by several keV to higher or lower energies, and transitions from the log-parabolic PED into the power-law one and/or vice versa. Such behavior could be related to the passage of a shock front through the regions with spatial scales $l \lesssim 10^{14}$ cm and significantly stronger turbulence, separated by the region with less extreme physical properties (magnetic field strength, particle number density, bulk Lorentz factor, etc.). Our detections show the viability of the

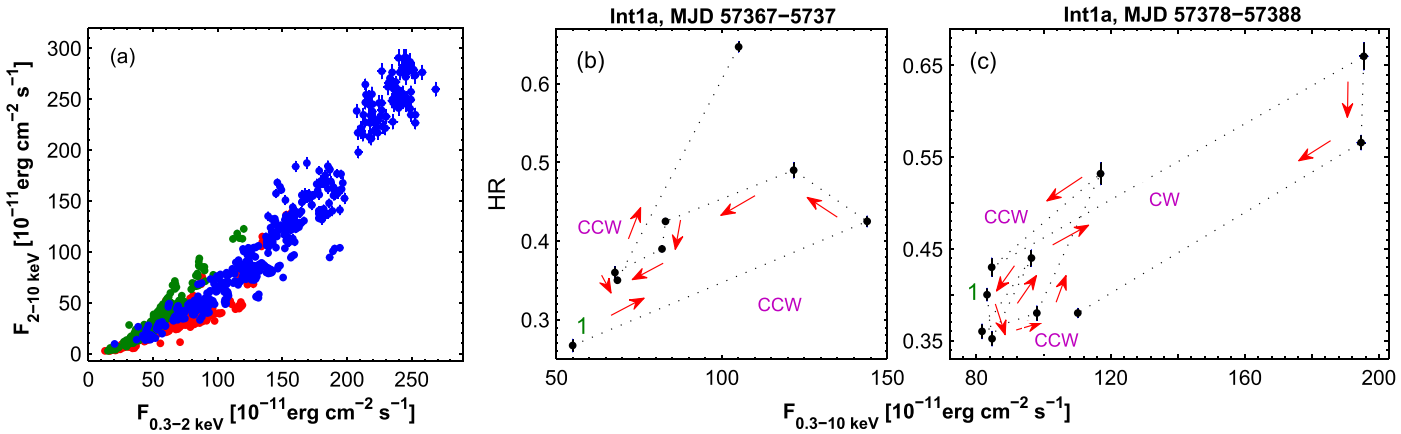

Figure 16. Panel (a): scatter plot with de-absorbed 0.3–2 and 2–10 keV fluxes. Subsequent panels: spectral hysteresis patterns in different subintervals. In each HR–flux plane, the starting point is denoted by "1." The complete set of subintervals is available in an online figure set (8 images).

(The complete figure set (8 images) is available.)

simulations of Mizuno et al. (2014), yielding a strong turbulence amplification on extremely small spatial scales in the shocked jet medium.

Stochastic acceleration scenarios predict the presence of the E_p–b anticorrelation (Tramacere et al. 2009). However, the latter was not detected at the 99% confidence level in interval 1 and was weak during intervals 1–3 (see Table 9 and Figure 9(b)). This correlation is deduced from the relation $\ln E \propto 2\ln\gamma_p + 3/(5b)$ (Tramacere et al. 2009), where γ_p is the PED peak energy. Note that the significant difference in the γ_p values, corresponding to the different X-ray flares, may result in a large scatter of the data points in the E_p–b plane or even the destruction of the anticorrelation. Furthermore, this correlation is also predicted for EDAP through $\log E \sim 3/(10b)$ (Chen 2014), and since this relation shows a different slope compared to the stochastic case, the joint operation of these mechanisms can yield a large scatter in the E_p–b plane and weaken the anticorrelation.

We found a positive $F_{0.3-10keV}$–E_p correlation during intervals 1–3, i.e., a trend of shifting the synchrotron SED peak to higher energies with rising X-ray flux (see Figure 9(g)). Tramacere et al. (2009) demonstrated that as the peak energy of the emission increases, the cooling timescale shortens and can compete with the acceleration timescales. It is then possible to observe a bias in the E_p–b relation (weakening the anticorrelation), since the cooling timescale is shorter than that of EDAP or stochastic acceleration.

Note that the anticorrelation between the 0.3–10 keV and radio variabilities, discussed above and explained as resulting from the shifting of the PED peak with a rising X-ray flux (corroborated by our finding of the positive $F_{0.3-10\ keV}$–E_p correlation), is expected in the framework of stochastic acceleration with a narrow initial energy distribution having a mean energy significantly higher than the equilibrium energy (Katarzynski et al. 2006). Presumably, such a physical condition was not the case for some X-ray flares when no declining radio brightness was observed. Moreover, since there were some flares with a negative a–b trend, this result hints at the low initial energies of the accelerating particles during those events.

In the case of the low spectral curvature, the electron volume density n_e is expected to be higher, yielding a brighter IC peak within the SSC scenario (Massaro et al. 2011b). Since the source generally shows its IC peak at the TeV frequencies (see, e.g., Acciari et al. 2011), lower VHE states are expected along with the high spectral curvatures. In fact, during the majority of the XRT observations with $b > 0.4$, Mrk 421 was not detectable with 3σ significance with FACT or showed excess rates lower than the mean value during 2015 December–2018 April. However, there were two exceptions showing higher VHE states along with $b > 0.4$ (MJD 57,388 and 57,548). On the other hand, the source was not detectable or showing low VHE states during some time intervals with predominantly low curvatures (e.g., MJD 57,408–57,486 and 58,147–58,162). These instances demonstrate that the one-zone SSC scenario was not always acceptable for our target in the presented period.

4.3.3. Spectral Loops

In the Bohm limit, the first-order Fermi mechanism yields an electron acceleration timescale $\tau_{FI} \approx 10200(c/v_{sh}^2)\sqrt{\gamma^2-1}\,(B/1G)^{-1}$, where v_{sh} is the shock speed (Tammy & Fuffy 2009). For a 1-G field, relativistic shock ($v_{sh} \rightarrow c$), and $\gamma \lesssim 10^4$, this timescale will be a few milliseconds or shorter. In that case, the acceleration and injection of electrons into the emission zone will be instantaneous, and a clockwise (CW) evolution of the X-ray flare in the plane $F_{0.3-10\ keV}$–HR is expected, making the spectrum progressively harder in the brightening phase of the source due to the emergence of a flaring component starting at hard X-rays (Tramacere et al. 2009). Although the de-absorbed soft 0.3–2 keV and hard 2–10 keV fluxes showed strong or very strong cross-correlations during intervals 1–3 (Figure 16(a) and Table 11), the latter underwent a higher variability in each interval (see Table 3 for the corresponding F_{var} and $\Re$ values), and the hysteresis patterns were clearly evident in the $F_{0.3-10\ keV}$–HR plane. The CW loops, expected in the case of EDAP, are evident in Figures 16(c)–(n), (p), and (r)–(u) during the various short- and longer-term flares discussed in Section 3.1. Two CW loops were also detected on intraday timescales (Figures 16(w) and (y)).

However, EDAP cannot be considered instantaneous in the case of significantly weaker magnetic fields, frequently inferred from the one or multizone SSC modeling of Mrk 421 ($B \lesssim 0.05$ G; see, e.g., Alecsic et al. 2012; Abeysekara et al. 2017). Furthermore, no instantaneous injection is expected for the hadronic content in the emission zone whose acceleration timescales are ~1000 times longer than for electrons (Tammy & Fuffy 2009). Note that the latter is more naturally compatible with the hard γ-ray spectra characterized by the photon index $\Gamma \lesssim 1.8$ (Mannheim 1993; Shukla et al. 2016), and such spectra were frequently recorded during the LAT observations in the presented period (as hard as $\Gamma_{\rm min} = 1.26 \pm 0.13$). Consequently, EDAP will be more gradual than instantaneous, X-ray flares will propagate from low energies to high energies, and counterclockwise (CCW) spectral evolution should be observed (Tammy & Fuffy 2009). Such behavior was also frequently observed in intervals 1–3 (see Figures 16(b)–(e), (g)–(j), (o)–(t), and (v)). Note that the slow, gradual acceleration and CCW loops are also expected during the stochastic acceleration in the jet region with low magnetic field and high matter density (Virtanen & Vainio 2005). On the contrary, this timescale can be much shorter and even instantaneous in the purely or mainly lepton plasma if the matter density is low and high magnetic fields are presented. In such a situation, CW-type loops can develop, although this requires quite ideal turbulence conditions with particle-scattering waves moving in opposite directions over a sufficiently long length scale (Tammy & Fuffy 2009).

4.3.4. Power-law Spectra

Along with EDAP and stochastic mechanisms, there could be other "competing" processes acting in the emission zone and weakening the observed $E_{\rm p}$–b correlation. Namely, the first-order Fermi process can yield a power-law PED when the magnetic field properties are variable, and its confinement efficiency becomes independent of the particle's energy for some time intervals. Note that 9.6% of the 0.3–10 keV spectra showed a simple power-law distribution of the photons with frequency, and they were observed mostly in higher X-ray states. This percentage was at an unprecedented high during 2005–2008 (27.5%), and the power-law spectra were observed most frequently during the densest XRT campaign in 2006 June 15–25, although they were recorded in any brightness states shown by the source in that period (Kapanadze et al. 2018a). A higher percentage (13%) and no clear trend with brightness were also observed during 2013 January–May (Kapanadze et al. 2016). On the contrary, the periods 2009–2012 and 2013 November–2015 June were characterized by significantly fewer occurrences of power-law spectra (4.9%–6.7%; Kapanadze et al. 2017a, 2018b).

Hard power-law PEDs with slopes $p < 2$ can be established by relativistic magnetic reconnection, expected to operate efficiently in highly magnetized plasma with the magnetization parameter $\sigma \gtrsim 10$ (Sironi & Spitkovsky 2014). However, the simulated broadband SEDs obtained by Petropoulou et al. (2016) for the cases $\sigma = 10$–50 differ significantly from those of Mrk 421 constructed using the data obtained during the different MWL campaigns (Alecsic et al. 2012; Balocovic et al. 2016; Abeysekara et al. 2017, etc.), particularly in the MeV–TeV energy range.

4.3.5. The Position of the Synchrotron SED Peak and Variable Turbulence Spectrum

During 2015 December–2018 April, only 15% of the spectra showed $E_{\rm p} > 2$ keV, i.e., peaking at the hard X-ray frequencies (taking the error ranges into account). This percentage is significantly lower than that shown by Mrk 421 during 2005–2008 (24%; Kapanadze et al. 2018a), and a higher occurrence of such spectra was also recorded during 2009–2012 (17%; Kapanadze et al. 2018b). Note that the spectra with $E_{\rm p} > 2$ keV were mostly concentrated in the subperiods 2006 April–July, 2008 March–June, 2009 November, and 2010 January–May. Due to the position of the synchrotron SED peak at higher frequencies, BAT frequently detected the source with 5σ confidence in the aforementioned time intervals: the BAT-band photons are generally of synchrotron origin in the HBL sources, and no significant contribution from the IC photons is found, in contrast to the low-energy-peaking BLLs (LBLs; e.g., OJ 287; see Kapanadze et al. 2018c).

On the other hand, the periods 2013 January–May and 2013 November–2015 June were characterized by a significantly lower occurrence of hard X-ray-peaking spectra (2% and 5%, respectively; see Kapanadze et al. 2016, 2017a). Note that the percentage of the spectra with $E_{\rm p} > 2$ keV was significantly higher for 1ES 1959+650 in 2016 January–August (48%) and 2016 August–2017 November (28%; Kapanadze et al. 2018d, 2018e). The highest value of this parameter was 12.80 ± 0.86 keV. However, a more extreme case with 94% spectra with the synchrotron peaks in the X-rays was recorded for Mrk 501 during the extended X-ray flaring activity in 2014 March–October (Kapanadze et al. 2017b). In that period, the maximum value $E_{\rm p}^{\rm max} = 20.96 \pm 2.81$ keV, and there was unprecedented spectral behavior in 1997 April when the synchrotron SED peak position underwent a shift by at least two orders of frequency and moved beyond 100 keV (Tavecchio et al. 2001). For our target, the most extreme SED position was observed on 2006 April 22 with $E_{\rm p}^{\rm max} = 26^{+19}_{-8}$ keV, obtained by Tramacere et al. (2009) from the joint fit of the log-parabolic model with the XRT and BAT spectra. Although the same authors reported more extreme cases, $E_{\rm p} > 100$ keV, from the 2006 April–June observations, our thorough analysis of these spectra showed insignificant spectral curvature and a good fit with a simple power law (Kapanadze et al. 2018a).

Figure 9(h) demonstrates a positive $\log E_{\rm p}$–$\log S_{\rm p}$ correlation with a slope of 0.63 ± 0.08—the value of the exponent α in the relation $S_{\rm p} \propto E_{\rm p}^{\alpha}$. This relation was predicted by the simulations of Tramacere et al. (2011) corresponding to the case when the momentum-diffusion coefficient D is variable during stochastic acceleration of the X-ray-emitting electrons. Consequently, there should be a transition from the Kraichnan spectrum of the turbulence with the exponent $Q = 3/2$ into the "hard sphere" spectrum ($Q = 2$). In the latter regime, the scattering and acceleration timescales are independent of the particle energy. During the transition, the synchrotron SED follows the expectation of a lower curvature for the harder turbulence spectra (Tramacere et al. 2011). On average, the lowest curvatures were observed in interval 3, which shows the strongest $\log E_{\rm p}$–$\log S_{\rm p}$ correlation during 2015 December–2018 April (see Table 9). These results can serve as another confirmation of the stochastic acceleration of particles in that period.

4.3.6. LAT-band Spectral Properties and Possible Jet–Star Interaction

The photon indices corresponding to the softer $\Gamma_{0.3-2\mathrm{GeV}}$ and harder $\Gamma_{2-300\mathrm{GeV}}$ LAT bands showed a weak cross-correlation during 2015 December–2018 April (see Figure 15(b) and Table 9). On some occasions, the index $\Gamma_{2-300\mathrm{GeV}}$ was lower than the 0.3–2 GeV one, which can be related to the soft gamma-ray excess at energies of several hundred MeV. One of the possible explanations consists of a star–jet interaction, expected in the blazars hosted by elliptical galaxies (including Mrk 421; see Scarpa et al. 2000). These galaxies may have a population of red giants surrounding the blazar jet and can carry large wind-blown bubbles into the jet, leading to gamma-ray emission through bubble–jet interactions (Torres-Alba & Bosch-Ramon 2019). Note that those instances, characterized by a spectral hardening with energy, are mostly observed in the period 2016 April–August, while no opposite spectral trend was observed during that time (see Figure 15(e) and Table 12). The simulations of Torres-Alba & Bosch-Ramon (2019) have shown that the IC emission resulting from the jet–bubble interaction is negligible ($L_{\mathrm{IC}} \sim 10^{40}\,\mathrm{erg\,s^{-1}}$), while that generated by the synchrotron mechanism can make a significant contribution to the MeV energy budget ($L_{\mathrm{IC}} \sim 10^{44}\,\mathrm{erg\,s^{-1}}$; see Alecsic et al. 2012 for comparison). In the latter case, the equipartition value of the magnetic field and acceleration efficiency $\xi \gtrsim 0.1$ are required.

In 17 cases, the index $\Gamma_{2-300\mathrm{GeV}}$ was higher than its lower-energy "counterpart" (the data points situated below the red dashed line in Figure 15(b); see Figure 15(f) for the corresponding SEDs). These cases could be related to the upscatter of X-ray photons to the 2–300 GeV energy range in the K–N regime, yielding a steepening of the corresponding photon spectrum with respect to that established in the 0.3–2 GeV range by means of the Thompson upscattering of the optical–UV photons (Kapanadze et al. 2018e). Finally, eight out of 23 LAT-band SEDs, where the difference between the $\Gamma_{0.3-2\mathrm{GeV}}$ and $\Gamma_{2-300\mathrm{GeV}}$ photon indices did not exceed the error ranges, were very hard, and their origin could be related to the hadronic contribution to the 0.3–300 GeV energy range (as suggested by Shukla et al. 2016).

5. Summary

In this paper, we have presented the spectral and timing results obtained during the intensive *Swift*-XRT and MWL observations of Mrk 421 in 2015 December–2018 April. The main results of our study are as follows.

1. Similar to the previous years, the source exhibited strong and erratic X-ray variability (without any quasi-periodicity). The most extreme behavior was recorded during 2017 December–2018 February when a long-term flare, lasting more than 2 months, was superimposed by short-term ones during which the 0.3–10 keV flux exceeded a level of $5 \times 10^{-9}\,\mathrm{erg\,cm^{-2}\,s^{-1}}$, similar to that recorded on 2008 June 12, and even higher states were observed during the giant outburst in 2013 April. This period was also characterized by several intraday flux doubling and halving events with $\tau_{\mathrm{d}} = 4.8$–18.9 hr, as well as by numerous lower-amplitude 0.3–10 keV IDVs with $F_{\mathrm{var}} = 0.20$–0.42, including extremely fast brightness fluctuations by 5%–18% within 180–600 s. Six other long-term flares of comparable duration but with lower amplitudes were evident during other parts of the period presented in this work.
2. The highest VHE states were recorded in 2018 January (coinciding with those in the XRT band), and the TeV-band variability mostly showed a good correlation with the X-ray one, although there were several exceptions when the VHE flux showed a decline or low states during the fast X-ray flare or the X-ray and VHE peaks were separated by a time interval of ∼1 day or longer, posing problems for one-zone SSC scenarios. In other spectral ranges, Mrk 421 exhibited a relatively different behavior: there was only a weak positive F_{XRT}–F_{LAT} correlation, and the highest 0.3–300 GeV states were recorded about 2 yr earlier than the X-ray ones, while the source exhibited only a moderate LAT-band flaring activity, along with the strongest X-ray flares recorded in interval 3a. Similarly, the highest optical–UV states were observed during 2016 January–February, and they were significantly lower 2 yr later when the source showed its highest X-ray activity. Consequently, the latter was anticorrelated with the UVOT-band variability, and a similar $F_{0.3-10\mathrm{keV}}$–F_{15GHz} relation was observed during the entire 2015 December–2018 April period. Such MWL variability favors some earlier simulations of the second-order Fermi process, when a population of the accelerating electrons are characterized by a narrow initial distribution of energy having a mean value significantly higher than the equilibrium energy.
3. During intervals 1 and 3, the distributions of the de-absorbed 0.3–10 keV flux showed lognormality features, which could be indicative of the variability imprint of AD on the jet. However, the data from interval 2 and the highest X-ray states did not show the same property. Since interval 2 clearly shows a better fit with the Gaussian function, and since this period was characterized, on average, by lower X-ray states (see Section 3.1 and Table 3), a lack of lognormality could be related to weaker shocks through the jet compared to other periods (possibly due to weaker AD instabilities). The FACT and LAT-band fluxes showed lognormality features in all intervals, in contrast to the radio–UV observations. The 0.3–10 keV IDVs were observed significantly more frequently during higher X-ray states and did not exhibit a lognormality. This result favors the "shock-in-jet" scenario. The longer-term flares may result from the propagation and evolution of relativistic shocks through the jet. The shock appearance could be related to an abrupt increase of the collimation rate at the jet base owing to some processes in the AD, yielding a lognormal flaring behavior on longer timescales.
4. Along with the strong flux variability, the source also exhibited an extreme spectral behavior. The 0.3–10 keV spectra generally showed their best fits with the log-parabolic model, yielding wide ranges of the curvature parameter $b = 0.07(0.05)$–$0.48(0.04)$ and photon index at 1 keV $a = 1.63(0.03)$–$2.92(0.02)$. The position of the synchrotron SED peak underwent extreme variability on various timescales between the energies $E_{\mathrm{p}} < 0.1$ keV (the UV frequencies) and $E_{\mathrm{p}} > 15$ keV, with 15% of the spectra peaking at hard X-rays. The synchrotron SED showed a positive correlation with the 0.3–10 keV flux: it shifted by several keV to higher energies during the

flaring phases and moved back along with brightness drops, exhibiting the most violent IDV by several keV during the strongest X-ray flares. Of the spectra, 33% were harder than $a = 2$, and the energy spectral shape generally followed a "harder-when-brighter" trend (except for some short time intervals with the opposite trend, explained by the emergence of a new soft X-ray component in the emission zone). The photon index varied on diverse timescales with variations from $\Delta a = 0.08$–0.23 within 0.13–0.28 hr to $\Delta a = 0.66$–1.07 in 3–27 days. Of the spectra, 9.6% were fitted well with a simple power law, with photon indices $\Gamma = 1.79$–2.91 and strongly following the "harder-when-brighter" trend. The source mostly showed a low spectral curvature ($b \sim 0.1$–0.3) and an anticorrelation $E_{\rm p}$–b, as predicted for the efficient stochastic acceleration of X-ray-emitting electrons by magnetic turbulence. Moreover, the source showed a positive a–b correlation, expected within the EDAP scenario, although it was weak, possibly due to the "competition" with other types of acceleration mechanisms and cooling processes not displaying the same correlation.

5. The 0.3–10 keV spectra showed a relation $S_{\rm p} \propto E_{\rm p}^{\alpha}$, where $\alpha \sim 0.6$, which demonstrates a transition from the Kraichnan-type turbulence spectrum into the "hard sphere" one due the variability of the momentum-diffusion coefficient. This result corroborates the importance of stochastic acceleration in the presented period. Our study of the spectral hysteresis patterns in the flux–HR plane shows the patterns of both the instantaneous injection and the gradual acceleration of X-ray-emitting electrons owing to first- and second-order Fermi processes.
6. The source frequently showed very hard 0.3–300 GeV spectra, predicted for a hadronic contribution to the HE emission. On some occasions, the corresponding SED showed a soft γ-ray excess, possibly owing to the jet interaction with a wind-blown bubble from a nearby red giant. This suggestion is corroborated by the fact that the MeV-excess SEDs mostly belong to the period 2016 April–August. On the contrary, there was a softening in the 2–300 GeV energy range compared to the 0.3–2 GeV spectrum, possibly due to the upscatter of X-ray photons in the 2–300 GeV energy range in the K–N regime. This may yield a steepening of the corresponding photon spectrum with respect to the 0.3–2 GeV range, corresponding to the Thompson upscatter of the optical–UV photons.

P.R. acknowledges the contract ASI-INAF I/004/11/0. We acknowledge the use of public data from the *Swift* data archive. This research has made use of the XRTDAS software, developed under the responsibility of the ASDC, Italy, and the data from the OVRO 40 m monitoring program, which is supported in part by NASA grants NNX08AW31G and NNX11A043G and NSF grants AST-0808050 and AST-1109911. We thank the FACT collaboration for making their analysis results publicly available. Finally, we thank the anonymous referee for useful comments and suggestions that helped to improve the quality of the paper.

ORCID iDs

B. Kapanadze https://orcid.org/0000-0002-7146-6751
S. Vercellone https://orcid.org/0000-0003-1163-1396
P. Hughes https://orcid.org/0000-0002-0691-3041
M. Aller https://orcid.org/0000-0003-2483-2103

References

Abdo, A. A., Ackermann, M., Ajello, M., et al. 2011, ApJ, 736, 131
Abeysekara, A. U., Archambault, S., Archer, A., et al. 2017, ApJ, 834, 2
Acciari, V. A., Aliu, E., Arlen, T., et al. 2011, ApJ, 738, 25
Acero, F., Ackermann, M., Ajello, M., et al. 2015, ApJS, 218, 23
Ahnen, M. L., Ansoldi, S., Antonelli, L. A., et al. 2016, A&A, 593, 91
Alecsic, J., Aleksić, J., Alvarez, et al. 2012, A&A, 542, 100
Alecsic, J., Ansoldi, S., Antonelli, L. A., et al. 2015a, A&A, 578, 22
Alecsic, J., Ansoldi, S., Antonelli, L. A., et al. 2015b, A&A, 576, 176
Anderhub, H., Backes, M., Biland, A., et al. 2013, Journ. of Instr, 8, P06008
Atwood, W. B., Abdo, A. A., Ackermann, M., et al. 2009, ApJ, 697, 1071
Balocovic, M., Paneque, D., Madejski, G., et al. 2016, ApJ, 819, 156
Barthelmy, S. D., Barbier, L. M., Cummings, J. R., et al. 2005, SSRv, 120, 143
Begelman, M. C., Fabian, A. C., & Rees, M. J. 2008, MNRAS, 384, L19
Bessel, M. S. 1979, PASP, 91, 589
Blazejowski, M., Blaylock, G., Bond, I. H., et al. 2005, ApJ, 630, 130
Böttcher, M., & Dermer, C. 2010, ApJ, 711, 445
Breeveld, A. A., Landsman, W., Hollandb, S. T., et al. 2011, AIPC, 1358, 373
Burrows, D. N., Hill, J. E., Nousek, J. A., et al. 2005, SSRv, 120, 165
Carnerero, M. I., Raiteri, C. M., Villata, M., et al. 2017, MNRAS, 472, 3789
Celotti, A., & Ghisellini, G. 2008, MNRAS, 385, 283
Cesarini, A. 2008, PhD Thesis, Nat. Univ. of Ireland Galway, https://aran.library.nuigalway.ie/handle/10379/3586
Chen, L. 2014, ApJ, 788, 179
Chevalier, J., Sanchez, D. A., Serpico, P. D., Lenain, J.-P., & Maurin, G. 2019, MNRAS, 484, 749
Dermer, C. D., Schlickeiser, R., & Mastichiadis, A. , 1992, A&A, 256, 27
Dorner, D., Ahnen, M. L., Bergmann, M., et al. 2015, arXiv:astro-ph/1502.02582
Falomo, R., Pian, E., Treves, A., et al. 2014, A&Arv, 22, 37
Fitzpartick, E. L., & Messa, D. 2007, ApJ, 663, 320
Foster, G. 1996, AJ, 112, 1709
Fukugita, M., Shimasaku, K., & Ichikawa, T. 1995, PASP, 107, 945
Gehrels, N., Chincarini, G., Giommi, P., et al. 2004, ApJ, 611, 1005
Giebels, B., & Degrange, B. 2009, A&A, 503, 797
Grossmann, A., & Morlet, J. 1984, SIAM J. Math. Anal., 15, 723
Kalberla, P. M. W., Burton, W. B., Hartmann, D., et al. 2005, A&A, 440, 775
Kapanadze, B., Dorner, D., Romano, P., et al. 2017a, ApJ, 848, 103
Kapanadze, B., Dorner, D., Romano, P., et al. 2017b, MNRAS, 469, 1655
Kapanadze, B., Dorner, D., Vercellone, S., et al. 2016, ApJ, 831, 102
Kapanadze, B., Dorner, D., Vercellone, S., et al. 2018e, ApJS, 238, 13
Kapanadze, B., Vercellone, S., Romano, P., et al. 2018a, ApJ, 854, 66
Kapanadze, B., Vercellone, S., Romano, P., et al. 2018b, ApJ, 858, 68
Kapanadze, B., Vercellone, S., Romano, P., et al. 2018c, MNRAS, 480, 407
Kapanadze, B., Vercellone, S., Romano, P., et al. 2018d, MNRAS, 473, 2542
Katarzynski, K., Ghisellini, G., Mastichiadis, A., Tavecchio, F., & Maraschi, L. 2006, A&A, 453, 47
Lomb, N. R. 1976, Ap&SS, 39, 447
Macomb, N., Akerfof, C. W., Aller, H. D., et al. 1995, ApJ, 449, L99
Mangalam, A. V., & Wiita, P. J. 1993, ApJ, 406, 420
Mannheim, K. 1993, A&A, 269, 60
Marscher, A. P. 2014, ApJ, 780, 87
Marscher, A. P., & Gear, W. K. 1985, ApJ, 298, 114
Massaro, F., Harris, D. E., & Cheung, C. C. 2011a, ApJS, 197, 24
Massaro, F., Paggi, A., & Cavaliere, A. 2011b, ApJ, 742, L32
Massaro, E., Perri, M., Giommi, P., & Nesci, R. 2004, A&A, 413, 489
Matsuoka, M., Kawasaki, K., Ueno, S., et al. 2009, PASJ, 61, 999
Mattox, J. R., Bertsch, D. L., Chiang, J., et al. 1996, ApJ, 461, 396
McHardy, I. 2008, in Proc. Blazar Variability across the Electromagnetic Spectrum Workshop (Trieste: PoS), 14
Mizuno, Y., Pohl, M., Hiemiec, J., et al. 2014, MNRAS, 439, 3490
Moretti, A., Campana, S., Mineo, T., et al. 2005, in Proc. SPIE, 5898, 360
Nilsson, K., Pasanen, M., Takalo, L. O., et al. 2007, A&A, 475, 199
Padovani, P., & Giommi, P. 1995, ApJ, 444, 567
Page, M., Kuin, N. P. M., Breeveld, A. A., et al. 2013, MNRAS, 436, 1684
Petropoulou, M., Giannios, D., & Sironi, L. 2016, MNRAS, 462, 3325

Pian, E., Türler, M., Fiocchi, M., et al. 2014, A&A, 570, 77
Poole, T. S., Breeveld, A. A., Page, M. J., et al. 2008, MNRAS, 383, 627
Rebillot, P. F., Badran, H. M., Blaylock, G., et al. 2006, ApJ, 641, 740
Richards, J. L., Max-Moerbeck, W., Pavlidou, V., et al. 2011, ApJS, 194, 209
Romano, P., Campana, S., Chincarini, G., et al. 2006, A&A, 456, 917
Romero, G. E., Cellone, S. A., & Combi, J. A. 1999, A&As, 135, 477
Roming, P. W. A., Kennedy, T. E., Mason, K. O., et al. 2005, SSRv, 120, 95
Rybicki, G. B., & Lightman, A. P. 1979, Radiative Processes in Astrophysics (New York: Wiley), 393
Saito, S., Stawarz, L., Tanaka, Y. T., et al. 2013, ApJ, 766, L11
Sandrinelli, A., Covino, S., Treves, A., et al. 2017, A&A, 600, 132
Scargle, J. D. 1982, ApJ, 263, 835
Scarpa, R., Urry, C. M., Falomo, R., Pesce, J. E., & Treves, A. 2000, ApJ, 532, 740
Shukla, A., Mannheim, K., Chitnis, V. R., et al. 2016, ApJ, 832, 177
Sinha, A., Sahayanathan, S., Acharya, B. S., et al. 2017, ApJ, 836, 83
Sinha, A., Shukla, A., Saha, L., et al. 2016, A&A, 591, 81
Sironi, L., & Spitkovsky, A. 2014, ApJ, 783, L21
Smith, P. S., Montiel, E., Rightley, S., et al. 2009, arXiv:0912.3621
Sokolov, A., Marscher, A. P., & McHardy, I. M. 2004, ApJ, 613, 725
Tammy, J., & Fuffy, P. 2009, MNRAS, 393, 1063
Tavecchio, F., Maraschi, L., Pian, E., et al. 2001, ApJ, 554, 725
Torres-Alba, N., & Bosch-Ramon, V. 2019, A&A, 623, 91
Tramacere, A., Giommi, P., Perri, M., Verrecchia, F., & Tosti, G. 2009, A&A, 501, 879
Tramacere, A., Massaro, E., & Taylor, A. M. 2011, ApJ, 739, 66
VanderPlas, J. T. 2018, ApJS, 236, 16
Vaughan, S., Edelson, R., Warwick, R. S., & Uttley, P. 2003, MNRAS, 345, 1271
Virtanen, J. J. P., & Vainio, R. 2005, ApJ, 621, 313